

May 2022

Stability Analysis and Parameters Design of the Voltage Source Inverter with LC Filter

Hongzhen Zhang
University of Wisconsin-Milwaukee

Follow this and additional works at: <https://dc.uwm.edu/etd>



Part of the [Electrical and Electronics Commons](#)

Recommended Citation

Zhang, Hongzhen, "Stability Analysis and Parameters Design of the Voltage Source Inverter with LC Filter" (2022). *Theses and Dissertations*. 3098.
<https://dc.uwm.edu/etd/3098>

This Thesis is brought to you for free and open access by UWM Digital Commons. It has been accepted for inclusion in Theses and Dissertations by an authorized administrator of UWM Digital Commons. For more information, please contact scholarlycommunicationteam-group@uwm.edu.

STABILITY ANALYSIS AND PARAMETERS DESIGN OF THE VOLTAGE
SOURCE INVERTER WITH LC FILTER

by

Hongzhen Zhang

A Thesis Submitted in
Partial Fulfillment of the
Requirements for the Degree of

Master of Science

in Engineering

at

The University of Wisconsin-Milwaukee

May 2022

ABSTRACT

STABILITY ANALYSIS AND PARAMETERS DESIGN OF THE VOLTAGE
SOURCE INVERTER WITH LC FILTER

by

Hongzhen Zhang

The University of Wisconsin-Milwaukee, 2022
Under the Supervision of Dr. Robert M Cuzner

Voltage source inverters (VSI) are widely used in many applications. In this thesis, the stability of the LC-type single-phase off-grid inverter is investigated and the emphasis is focused on how to extend the effective damping region.

The harmonics resonance is the main factor affecting the stability of the system. To deal with this problem, the stability of the system with passive damping is investigated. Aiming at the problem that passive damping methods introduce the power loss, Active damping methods are proposed. Considering the system with traditional inductor-current feedback active damping cannot be stable when resonance frequency is close to $f_s/6$, a lag compensation method based on the all-pass filter is proposed. To design the parameters more conveniently, a design guideline is given and the simulation verifies the effectiveness of this method. Traditional inductor-current active damping can keep the system stable when $f_r < f_s/6$ and all-pass filter can stabilize the system when f_r is close to $f_s/6$. However, the effective damping region is still narrow. To extend the stable region, an improved inductor-current feedback active damping based on negative first-order low-pass filter is proposed. This method can

extend the effective damping region to f_c , where $f_c \in (f_s/3, f_s/2)$. Simulation verifies the validity of this method.

© Copyright by Hongzhen Zhang, 2022
All Rights Reserved

TABLE OF CONTENTS

Chapter 1 Introduction..... 1

 1.1 Background..... 1

 1.2 Research status of the damping of the output LC filter2

 1.3 Contribution3

 1.4 Thesis Structure4

Chapter 2 Stability Analysis of the Inverter with Single Voltage Loop Control System 6

 2.1 Introduction.....6

 2.2 Model of the inverter with single loop voltage control.....6

 2.3 Nyquist stability criterion in open loop bode diagram.....10

 2.4 Stability analysis of Inverter with single loop voltage control10

 2.5 Passive damping..... 12

 2.6 Parameters design 15

 2.7 Simulation and results.....16

 2.8 Conclusion19

Chapter 3 Stability Analysis of the Inverter with Inductor-Current Feedback Active Damping.....21

 3.1 Introduction.....21

 3.2 Model of the inverter with Inductor-Current Feedback.....21

 3.3 Stability analysis24

 3.4 Parameters design method28

3.5 Simulation and results.....	29
3.6 Conclusion	32
Chapter 4 A Lag Compensation Method Based on All-Pass Filter	34
4.1 Introduction.....	34
4.2 Stability analysis	34
4.2.1 Number of unstable poles	34
4.2.2 -180° crossing	36
4.3 Lag compensation methods.....	39
4.3.1 Notch filter.....	39
4.3.2 All-pass filter.....	40
4.4 Parameters design	41
4.5 Design guideline	44
4.6 Simulation.....	45
4.7 Conclusion	48
Chapter 5 A Lag Compensation Method Based on Negative First-Order Low-Pass Filter	50
5.1 Introduction.....	50
5.2 Traditional inductor-current feedback active damping	50
5.3 Improved capacitor-current feedback active damping with negative first-order low-pass filter.....	52
5.4 Stability analysis	54
5.4.1 The effect of H on poles.....	55

5.4.2 -180° crossing	55
5.5 Parameters design	56
5.6 Simulation	57
5.7 Conclusion	62
Chapter 6 Thesis conclusion.....	63
References	65

LIST OF FIGURES

Figure 1.1 Single-phase VSI system with an output LC filter 1

Figure 1.2 Bode diagram of LC-type inverter system 2

Figure 2.1 Topology of LC type inverter with single voltage loop control 7

Figure 2.2 Control scheme of the inverter with single loop voltage control in hybrid domain..... 8

Figure 2.3 Equivalent control scheme of the inverter with single loop voltage control in s domain..... 9

Figure 2.4 Bode diagram of Scenario 1 and Scenario 2..... 12

Figure 2.5 Four types of passive damping method 13

Figure 2.6 Frequency characteristics of LC filters with 4 basic passive damping methods..... 14

Figure 2.7 Output voltage waveform of Case I simulation model..... 17

Figure 2.8 Output voltage spectrum of Case I simulation model 18

Figure 2.9 Output voltage waveform of Case II simulation model..... 18

Figure 2.10 Output voltage waveform of Case III simulation model 18

Figure 2.11 Output voltage spectrum of Case III simulation model..... 19

Figure 2.12 Output voltage waveform of Case IV simulation model..... 19

Figure 2.13 Output voltage spectrum of Case IV simulation model..... 19

Figure 3.1 Topology of the LC type inverter with inductor-current feedback 21

Figure 3.2 Control scheme of the inverter with inductor-current feedback in hybrid domain..... 23

Figure 3.3 Equivalent control scheme of the LC-type off-grid inverter with inductor-current feedback in s domain23

Figure 3.4 Equivalent control scheme of the LC-type off-grid inverter with inductor-current feedback in z domain24

Figure 3.5 Pole map and the bode diagram of case 126

Figure 3.6 Pole map and the bode diagram of case 227

Figure 3.7 Pole map and the bode diagram of case 327

Figure 3.8 Value of k_{max} with the change of H 29

Figure 3.9 Output voltage and load current waveforms of Case A30

Figure 3.10 Output voltage spectrum of Case A30

Figure 3.11 Output voltage and load current waveforms of Case B31

Figure 3.12 Output voltage spectrum of Case B31

Figure 3.13 Output voltage and load current waveforms of Case C31

Figure 3.14 Output voltage spectrum of Case C32

Figure 4.1 The pole map and the bode diagram of scenario a36

Figure 4.2 Pole map and the bode diagram of scenario b37

Figure 4.3 Pole map and the bode diagram of scenario c37

Figure 4.4 Pole map and the bode diagram of scenario d38

Figure 4.5 The ideal bode diagram39

Figure 4.6 The bode diagram of Notch filter40

Figure 4.7 The bode diagram of all-pass filter41

Figure 4.8 The bode diagram of all-pass filter with $a = 0.424$ 42

Figure 4.9 The bode diagram of scenario c with all-pass filter.....42

Figure 4.10 the final bode diagram of scenario c with all-pass filter.....43

Figure 4.11 Pole map of the overall system when resonance frequency f_r are changed (changing from 90% of $f_s/6$ to 110% of $f_s/6$).....44

Figure 4.12 Design flowchart.....44

Figure 4.13 Output voltage waveform of the system without compensation46

Figure 4.14 Output voltage and load current waveforms of Case I47

Figure 4.15 Output voltage spectrum of Case I47

Figure 4.16 Output voltage and load current waveforms of Case II.....47

Figure 4.17 Output voltage spectrum of Case II48

Figure 4.18 Output voltage and load current waveforms of Case III.....48

Figure 4.19 Output voltage spectrum of Case III.....48

Figure 5.1 Topology of the inverter with traditional inductor-current feedback.....50

Figure 5.2 Control scheme of the inverter with traditional inductor-current feedback in hybrid domain 51

Figure 5.3 Equivalent control scheme of the LC-type off-grid inverter with traditional inductor-current feedback in s domain.....51

Figure 5.4 Characteristics of R_{eq} and X_{eq} 52

Figure 5.5 Control scheme of the inverter with improved inductor-current feedback in hybrid domain 53

Figure 5.6 Control scheme of the inverter with improved inductor-current feedback in s domain53

Figure 5.7 Characteristic of R_{eq2} and X_{eq2} with $\lambda = 7.643 \times 10^{-5}$ 54

Figure 5.8 Pole map of $Den(z)$ with $\lambda = 7.643 \times 10^{-5}$ when H is changed (Changing from 0 to 9) 55

Figure 5.9 The bode diagram of $T_{oz}(z)$ with $\lambda = 7.643 \times 10^{-5}$ and $H = 1.2$ 56

Figure 5.10 the bode diagram of $T_{oz}(z)$ with $\lambda = 7.643 \times 10^{-5}$, $H = 1.2$ and $k_p = 0.015$ 57

Figure 5.11 The pole map and the bode diagram when f_r changes from $f_s/6$ to $5f_s/12$ 57

Figure 5.12 Output voltage and load current waveforms of Case 1 59

Figure 5.13 Output voltage spectrum of Case 1 59

Figure 5.14 Output voltage and load current waveforms of Case 2 60

Figure 5.15 Output voltage spectrum of Case 2 60

Figure 5.16 Output voltage and load current waveforms of Case 3 60

Figure 5.17 Output voltage spectrum of Case 3 61

Figure 5.18 output voltage and load current waveforms of Case 4 61

Figure 5.19 Output voltage spectrum of Case 4 61

Figure 5.20 Output voltage and load current waveforms of Case 5 62

Figure 5.21 Output voltage spectrum of Case 5 62

LIST OF TABLES

Table 2-1 Parameters of the off-grid inverter 12

Table 2-2 Parameters of the off-grid inverter and control parameters 16

Table 3-1 Unstable poles of the open loop transfer function26

Table 3-2 Parameters of the off-grid inverter28

Table 3-3 Control Parameters29

Table 4-1 The number of unstable poles35

Table 4-2 Parameters of the off-grid inverter and control parameters45

Table 5-1 Parameters of the off-grid inverter and control parameters58

ACKNOWLEDGEMENTS

Throughout the writing of this thesis, I have received a great deal of support and assistance.

Firstly, I would like to express my appreciation to my advisor, Dr. Robert M Cuzner, and Dr. David Yu. Dr. Cuzner has a comprehensive understanding of the power electronics and associated issues. Dr. Yu provided me a lot of assistance when I first came to UWM

Secondly, I would like to extend my thankful gratitude to my friend Jiangdan Ye. The content of chapter 4 is cooperated by us and I learned a lot from him. Every time I encounter a problem that I fail to deal with, he can always give me instant feedback. It is his insightful feedback that motivated me to think deeper and improve the quality of my work.

Thirdly, I would like to thank Dr. Yi Hu and Dr. Benjamin C Church. Thank you for accepting my invitation to be part of my thesis committee. Thank you for your insightful remarks and helpful recommendations.

Fourthly, I would also like to thank Mr. Yu Lu, Mr. Jingnan Liu, and Mrs. Zhiqin Qiang who are the students pursuing their doctor's degrees. They provided me with lots of suggestions and advice on my thesis.

Finally, I would like to thank my parents far in my homeland for their full support.

This work is in part by China Scholarship Council award CSC NO. 202106050003, Office of Naval Research Award No. N00014-20-1-2667, and National Science Foundation Grant No. 1939124.

Chapter 1 Introduction

1.1 Background

Due to the shortage of fossil fuels and their environmental consequences, attention has been focused on distributed generation (DG) systems where voltage source inverters (VSI) are widely used [1]. Depending on the various power levels of AC loads, inverters can be roughly divided into low-power single-phase inverters and high-power three-phase inverters. The single-phase inverter is most common in residential areas, whereas the three-phase inverter is widely used in places that require greater power, such as industrial buildings and enterprises [2]. In this thesis, the attention is focused on the single-phase inverter.

To guarantee the high-quality AC voltage is delivered to the load, an LC-type low-pass filter is introduced between the inverter bridge and the load to filter out the switching harmonics [3]. **Figure 1.1** shows the single-phase VSI system with an output filter.

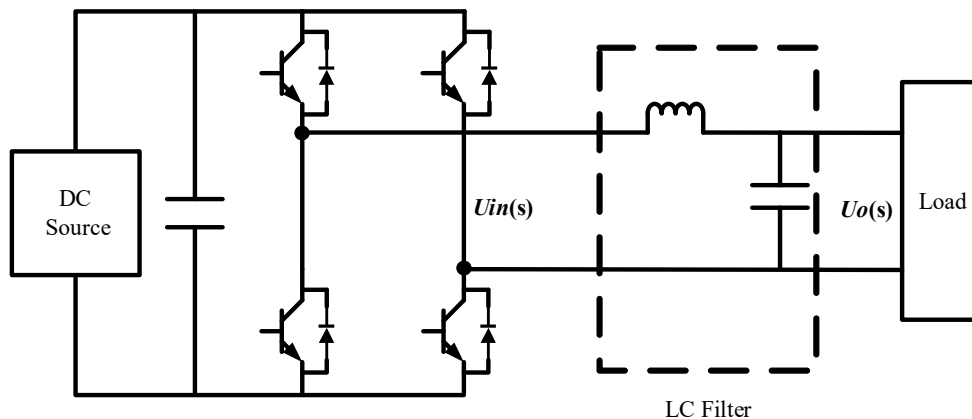


Figure 1.1 Single-phase VSI system with an output LC filter

The transfer function $G_{LC}(s)$ from the inverter output voltage $U_{in}(s)$ to $U_o(s)$

can be calculated as [4].

$$G_{LC}(s) = \frac{U_o(s)}{U_{in}(s)} = \frac{\omega_r^2}{s^2 + \omega_r^2} \quad (1.1)$$

Figure 1.2 shows the bode diagram of the LC-type inverter system under digital control when $G_{PR}(s)$ is simplified as k_p , which will be explained in detail in chapter 2. As it can be observed, a resonance peak and a phase jump of 180° exist at the resonance frequency f_r , which are the main factors affecting the stability of the system. This is because the resonance peak fails the system to satisfy the stable conditions based on the Nyquist stability criterion, which will be discussed in the following chapters.

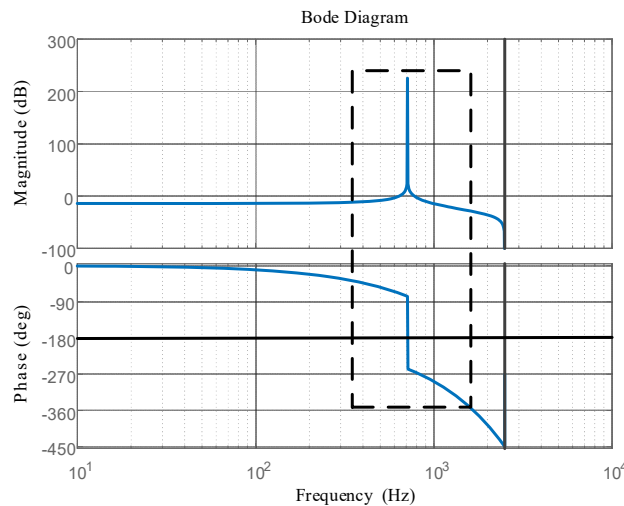


Figure 1.2 Bode diagram of LC-type inverter system

1.2 Research status of the damping of the output LC filter

The resonance peak affects the stability of the system [5]. Therefore, the suppression of harmonic resonance has received a lot of research interest, and numerous strategies for improving the stability of an LC-type VSI have been presented.

The techniques can be approximately divided into two categories: passive damping [6] and active damping [7]. Passive damping means that actual resistors are

connected in series or parallel with the filter components. This approach is straightforward to implement. However, the power loss through the resistor prohibits this strategy from being used, especially in high voltage applications [5]. To handle this problem, active damping is proposed, which can be realized by adjustments in the control loop. In [8], based on double loop control, the virtual resistor connected in series or parallel with the filter components can be derived from the transformation of a block diagram. However, the influence of the delay introduced by pulse width modulation (PWM) and digital control is not considered. [9] indicated that the delay is a significant factor affecting the stability which cannot be overlooked. [10] demonstrated that, considering the time delay, the inductor current inner loop can be equivalent to the virtual impedance in series with the inductor of the filter. According to the transfer function of the virtual impedance, it can be known that the resonance frequency affects the characteristic of the virtual resistor (the real part of virtual impedance) and only the positive resistor can damp the resonance peak. In [10], the stability of the system is analyzed when resonance frequency varies from 0 to $f_s / 4$. Unfortunately, the stability of the system is not investigated when resonance frequency equals $f_s / 6$ or exceeds $f_s / 4$.

1.3 Contribution

- Review the literature on the damping of resonance peak in detail
- Investigate the stability of the system under digital control when resonance frequency equals $f_s / 6$ and propose a lag compensation method based on all-pass filter.

- Propose an improved inductor-current feedback active damping based on Negative First-Order Low-Pass Filter to extend the effective damping region.
- Illustrate the effectiveness of the proposed approach in the case study

1.4 Thesis Structure

Chapter 1: The Research background and goal of the study are presented. Due to the shortage of fossil fuels and the popularity of renewable energy, it is necessary to draw attention to inverters. In this thesis, the emphasis is on the stability analysis and parameters design of a single-phase full-bridge LC-type inverter.

Chapter 2: The open loop transfer function of the inverter with single loop voltage control is derived from the Equivalent continuous model. According to the Nyquist stability criterion, the stable region and unstable region can be attained. For the unstable region, passive damping methods are proposed and the simulation results confirm the effectiveness of these methods.

Chapter 3: A kind of active damping approach is proposed and it can be realized by inductor-current feedback. The open loop transfer function of the inverter with inductor-current feedback active damping is derived from the z domain model. Based on the Nyquist stability criterion and Julius criterion, the stable conditions and parameters design method can be attained. The simulation results verify the effectiveness of this method.

Chapter 4: Based on the same model from chapter 3, the strict mathematical derivation in z domain is given to indicate the system cannot be stable when f_r equals $f_s / 6$. Then a lag compensation method based on all-pass filter is implemented to deal

with this problem. To design the parameters more conveniently, a design guideline is given. The simulations are conducted to confirm the effectiveness of the proposed approach.

Chapter 5: The system with traditional inductor-current feedback active damping can be stabilized when $f_r < f_s / 6$ which has been mentioned in chapter 3. To extend the effective damping region, an improved inductor-current feedback active damping based on Negative First-Order Low-Pass Filter is proposed. The simulation results conducted verify that this approach can extend the stable region to f_c , where $f_c \in (f_s / 3, f_s / 2)$.

Chapter 6: The conclusion of the thesis is given.

Chapter 2 Stability Analysis of the Inverter with Single Voltage Loop Control System

2.1 Introduction

This chapter introduces the power circuit and single voltage control loop of the off-grid inverter with LC filter. After understanding the derivation of each link, the expression of the open-loop transfer function is obtained. According to the stability analysis tool, Nyquist stability criterion, the stable region and unstable region have been attained. For the unstable region, passive damping approaches have been proposed and the simulation results verify the effectiveness of this method.

2.2 Model of the inverter with single loop voltage control

Figure 2.1 shows the topology and control loop of the inverter with LC filter. This system contains an ideal dc supply U_{dc} with constant voltage, a capacitor C_s , a single-phase full bridge VSI which consists of MOSFET $S1$, $S2$, $S3$, $S4$ and their respective reverse parallel diodes, and an LC filter. In **Figure 2.1**, L is the filter inductor, C is the filter capacitor, and the load resistor is in parallel with the filter capacitor to obtain AC power. Since the equivalent resistance of the elements can provide some suppression of the resonant peak, we neglect parasitic resistance on switching devices, diodes, inductors, capacitors, and transmission cables to obtain the worst condition of the system [5]. $I_L(s)$, $I_C(s)$, $I_o(s)$, $U_{inv}(s)$ and $U_o(s)$ are the inductor current, capacitor current, load current, inverter bridge side voltage and terminal voltage, respectively. In this paper, the switching frequency f_{sw} is equal to the sampling frequency f_s .

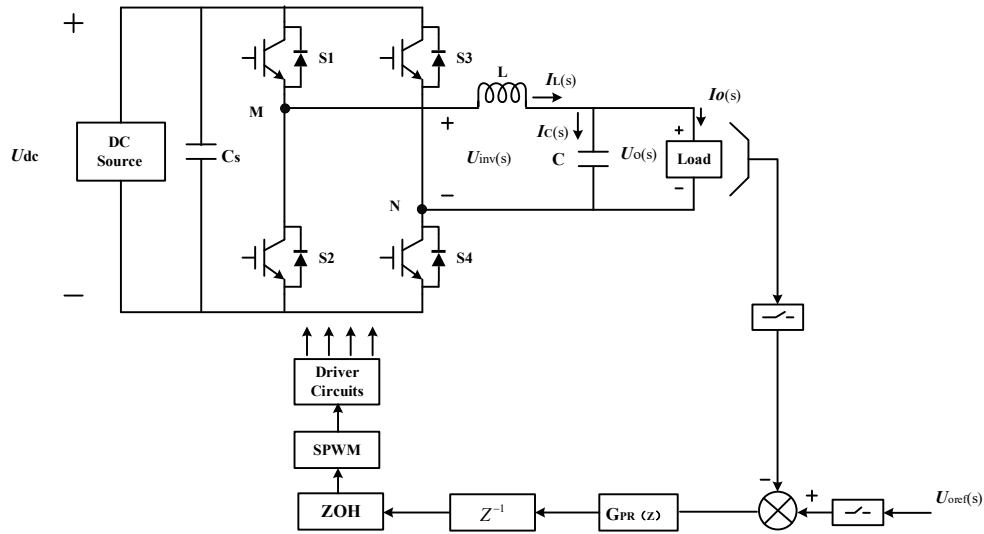


Figure 2.1 Topology of LC type inverter with single voltage loop control

The output voltage $U_o(s)$ is sampled to the digital signal processor via a sampling switch. $U_{oref}(s)$ is the reference voltage given by the closed-loop control system. Quasi Proportional-Resonant (QPR) compensator, as depicted in **Figure 2.1**, is implemented for the single-phase inverter to replace the conventional PI compensator. Compared with the PI control, PR control has two prominent benefits: the ability to track sinusoidal voltage signal with zero steady-state error and the ability to reject disturbance caused by oscillation effects [11]. $G_{PR}(s)$ is the continuous version of PR compensator which can be given by

$$G_{PR}(s) = k_p + \frac{k_r \omega_{cut} s}{s^2 + 2\omega_{cut} s + \omega_0^2} \quad (2.1)$$

where k_p and k_r are proportional gain constants and resonant gain constants respectively; ω_0 is the fundamental frequency of the reference signal which is 100π ; ω_{cut} is the bandwidth of the controller which is also known as cutoff frequency and the value is π .

Compared with other techniques for transfer function discretization, the prewarped

bilinear (Tustin) transformation is accurate in most applications [12]. Therefore, this method is applied to (2.1). The discrete version of $G_{PR}(s)$ can be expressed by $G_{PR}(z)$ [10], shown as follows

$$G_{PR}(z) = k_p + \frac{k_r \omega_{cut} \sin(\omega_0 T_s)}{2} \cdot \frac{z^2 - 1}{\omega_0 z^2 - 2\omega_0 \cos(\omega_0 T_s) z + \omega_0 + \omega_{cut} \sin(\omega_0 T_s) z^2 - \omega_{cut} \sin(\omega_0 T_s)} \quad (2.2)$$

Digital control is implemented in this single-phase inverter and it will introduce an inherent control delay which is made up of one sampling period from sampling and computation, and half sampling period from zero-order hold (ZOH) [13]. $G_D(s)$ and $G_D(z)$ refer to continuous version and discrete version of computation delay, which can be expressed respectively by

$$G_D(s) = e^{-sT_s} \quad (2.3)$$

$$G_D(z) = z^{-1} \quad (2.4)$$

$G_{ZOH}(s)$ is the continuous transfer function of ZOH, which is given by

$$G_{ZOH}(s) = \frac{1 - e^{-sT_s}}{s} \approx T_s e^{-0.5sT_s} \quad (2.5)$$

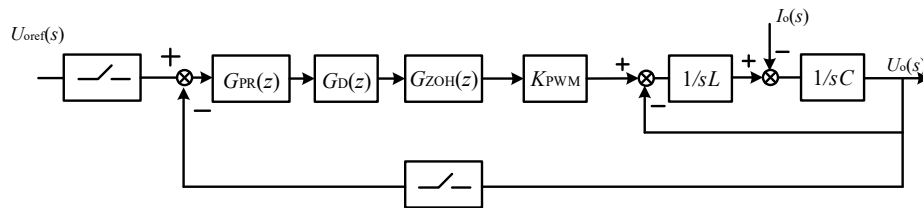
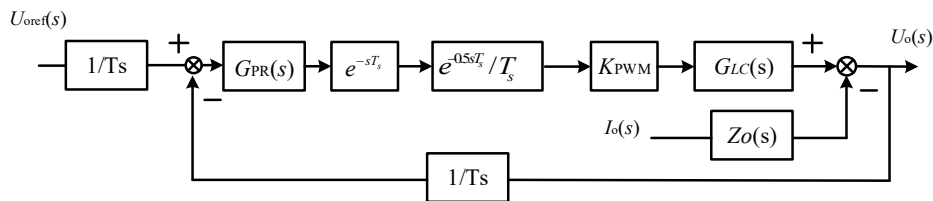
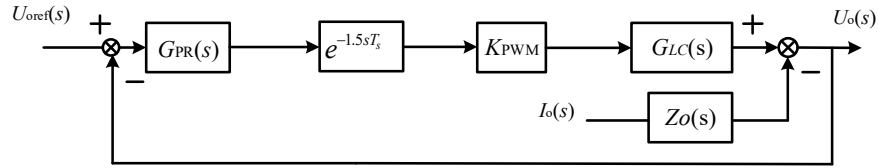


Figure 2.2 Control scheme of the inverter with single loop voltage control in hybrid domain



(a) Equivalent control scheme 1



(b) Equivalent control scheme 2

Figure 2.3 Equivalent control scheme of the inverter with single loop voltage control in s domain

Figure 2.2 shows the control scheme of the inverter in hybrid domain which can be obtained based on **Figure 2.1**. In order to reflect the effect of control delay more intuitively, the hybrid domain model is transformed into the continuous domain model to do s-domain analysis, which is shown in **Figure 2.3**. $1/T_s$ presents the continuous expression of the digital sampler [13].

Considering the volume of the filter under the same switching frequency, unipolar double-frequency sinusoidal pulse width modulation (UDF-SPWM) rather than bipolar SPWM (BSPWM) is applied for this inverter [14]. Compared with bipolar SPWM (BSPWM), the harmonics of output voltage with UDF-SPWM are mainly at twice the switching frequency, which can be filtered using a smaller size filter. The gain of the inverter is K_{PWM} by using average switch model [15].

$G_{LC}(s)$ is the transfer function of the LC filter [4], which can be given by

$$G_{LC}(s) = \frac{U_o(s)}{U_{inv}(s)} = \frac{\omega_r^2}{s^2 + \omega_r^2} \quad (2.6)$$

where ω_r is resonance frequency of the LC filter, which can be expressed as

$$\omega_r = \sqrt{\frac{1}{LC}} = 2\pi f_r \quad (2.7)$$

$Z_o(s)$ is the transfer function from load current $I_o(s)$ to capacitor voltage $U_o(s)$, which can be expressed as [16]

$$Z_o(s) = -\frac{U_o(s)}{I_o(s)} \Big|_{U_{inv}(s)=0} = \frac{s}{C(s^2 + \omega_r^2)} \quad (2.8)$$

However, the load will introduce some damping in the system. Accordingly, no-load conditions are the worst scenario that can be chosen as the object of study when studying the system stability. Based on previous analysis, the final open loop transfer function can be obtained as

$$T_o(s) = G_{PR}(s) \cdot K_{PWM} \cdot \frac{\omega_r^2}{s^2 + \omega_r^2} \cdot e^{-1.5sT_s} \quad (2.9)$$

2.3 Nyquist stability criterion in open loop bode diagram

Before doing the stability analysis, it is necessary to introduce the stability analysis tool, Nyquist stability criterion [17]. Due to the analysis in the bode diagram, the expression can be attended as

$$Z = P - 2(N^+ - N^-) \quad (2.10)$$

where Z represents the number of unstable poles of the closed loop transfer function, P represents the number of unstable poles of the open loop transfer function, N^+ and N^- represent the number of the positive and negative crossings of -180° with gains above 0 dB separately.

If Z equals 0, the system can be stable. Otherwise, the system cannot work stably.

2.4 Stability analysis of Inverter with single loop voltage control

Considering the resonant gain of the QPR compensator does not affect the signals whose frequencies are far away from its resonant frequency [15]. So, the resonant

controller is ignored for the simplicity of calculation, which means $G_{PR}(s)$ is regarded as k_p . The final open loop transfer function (2.9) can be changed into a simple form given by

$$T_o(s) = k_p \cdot K_{PWM} \cdot \frac{\omega_r^2}{s^2 + \omega_r^2} \cdot e^{-1.5sT_s} \quad (2.11)$$

As it can be seen, the number of unstable poles of $T_o(s)$ is zero, which means P equals zero.

$$|T_o(j\omega)| = \frac{k_p K_{PWM}}{|1 - LC\omega^2|} \quad (2.12)$$

$$\angle T_o(j\omega) = \begin{cases} -1.5T_s\omega = -3\pi T_s f, & f < f_r \\ -\pi - 1.5T_s\omega = -\pi - 3\pi T_s f, & f_r < f < f_N \end{cases} \quad (2.13)$$

To study the effects of different resonance frequency on the system stability, two different scenarios have been given in **Table 2-1** [10]. According to (2.13), the expression of phase frequency characteristic, when $f_r < f_s / 3$, the crossing of -180° happens at resonance frequency; when $f_s / 3 < f_r < f_s / 2$, the crossing of -180° line happens at $f_s / 3$. The corresponding bode diagram shown in **Figure 2.4** confirms the analysis. For scenario 1, based on the inequation, $k_p < |1 - LC(2\pi f_s / 3)^2| / K_{PWM}$, appropriate k_p could be chosen to void the negative crossing, which means $N^- = 0$ and the system will be stable. The resonance gain k_r can be determined based on the steady-state error. For scenario 2, the negative crossing could not be voided, even with k_p close to zero, since the denominator of (2.12) is zero when f equals f_r . Accordingly, it is necessary to implement the passive damping approach to provide some damping for the system with f equal to f_r , keeping the magnitude of the peak

below unit.

Table 2-1 Parameters of the off-grid inverter

Parameter	Scenario 1	Scenario 2
Inductor L	0.5 mH	1.0 mH
Capacitor C	10 μ F	50 μ F
Resonance frequency f_r	2251 Hz	712 Hz
The gain K_{PWM}	1	1
Sampling frequency f_s	5kHz	5kHz

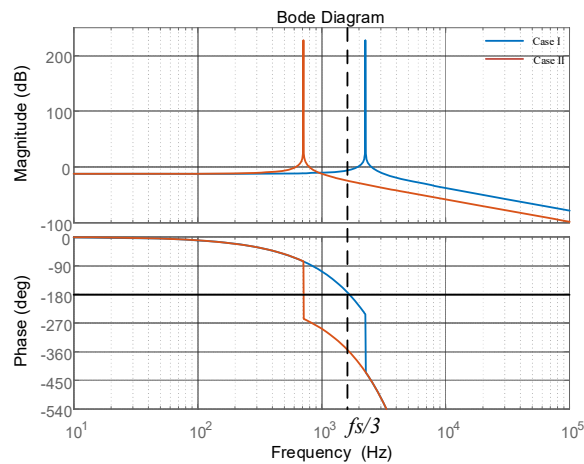
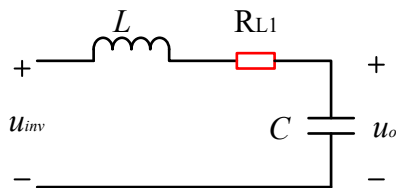


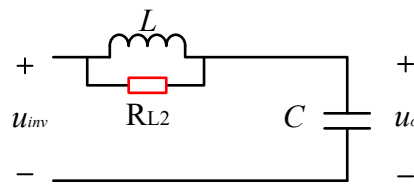
Figure 2.4 Bode diagram of Scenario 1 and Scenario 2

2.5 Passive damping

Four types of the most basic passive damping methods are shown in **Figure 2.7** [18].



(a) R in series with L



(b) R in parallel with L

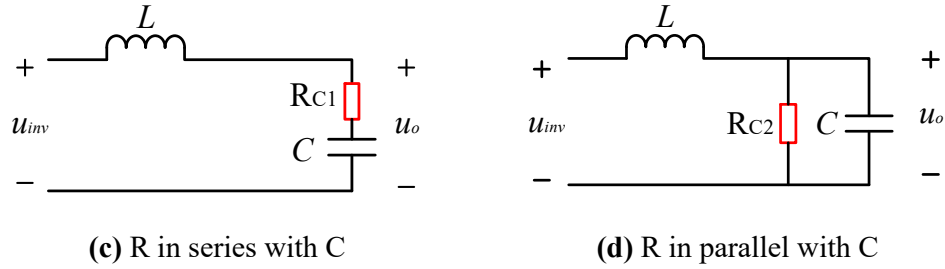


Figure 2.5 Four types of passive damping method

1. Resistor R_{L1} in series with Inductor L

According to **Figure 2.5 (a)**, $G_{LC-1}(s)$ is the transfer function from inverter side voltage $U_{inv}(s)$ to capacitor voltage $U_o(s)$, which can be expressed as

$$G_{LC-1}(s) = \frac{U_o(s)}{U_{inv}(s)} = \frac{1}{s^2 LC + R_{C1}Cs + 1} = \frac{\omega_r^2}{s^2 + \frac{R_{C1}}{L}s + \omega_r^2} \quad (2.14)$$

2. Resistor R_{L2} in parallel with Inductor L

According to **Figure 2.5 (b)**, $G_{LC-2}(s)$ is the transfer function from inverter side voltage $U_{inv}(s)$ to capacitor voltage $U_o(s)$, which can be expressed as

$$G_{LC-2}(s) = \frac{U_o(s)}{U_{inv}(s)} = \frac{Ls + R_{L2}}{s^2 LR_{L2}C + Ls + R_{L2}} = \frac{\frac{1}{R_{L2}C}s + \omega_r^2}{s^2 + \frac{1}{R_{L2}C}s + \omega_r^2} \quad (2.15)$$

3. Resistor R_{C1} in series with Inductor C

According to **Figure 2.5 (c)**, $G_{LC-3}(s)$ is the transfer function from inverter side voltage $U_{inv}(s)$ to capacitor voltage $U_o(s)$, which can be expressed as

$$G_{LC-3}(s) = \frac{U_o(s)}{U_{inv}(s)} = \frac{RCs + 1}{s^2 LC + RCs + 1} = \frac{\frac{R}{L}s + \omega_r^2}{s^2 + \frac{R}{L}s + \omega_r^2} \quad (2.16)$$

4. Resistor R_{C2} in parallel with Inductor C

According to **Figure 2.5 (d)**, $G_{LC-4}(s)$ is the transfer function from inverter side voltage $U_{inv}(s)$ to capacitor voltage $U_o(s)$, which can be expressed as

$$G_{LC-4}(s) = \frac{U_o(s)}{U_{inv}(s)} = \frac{R_{C2}}{s^2 R_{C2} LC + Ls + R_{C2}} = \frac{\omega_r^2}{s^2 + \frac{1}{R_{C2}C}s + \omega_r^2} \quad (2.17)$$

To analyze the damping characteristics of the four passive damping methods in detail, the Bode diagrams of corresponding transfer functions from (2.14) to (2.17) are shown in **Figure 2.6**, respectively [18].

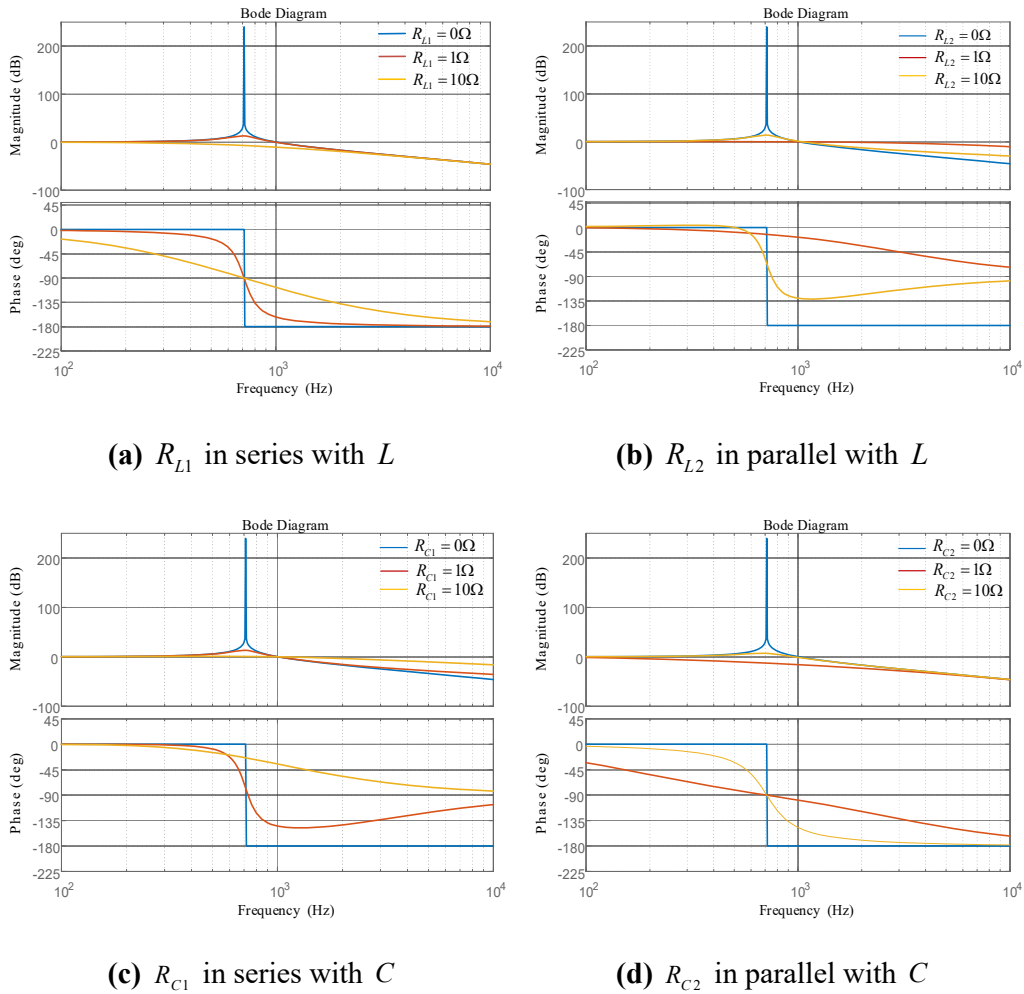


Figure 2.6 Frequency characteristics of LC filters with 4 basic passive damping methods

Figure 2.6 (a) shows the passive damping method for the resistor in series with the inductor. Note the resonant peak of the LC filter can be effectively damped and the resistance has no effect on the low frequency gain and high frequency harmonic attenuation capability of the filter.

Figure 2.6 (b) shows the passive damping method for the resistor in parallel with the inductor. Note the resonant peak of the LC filter could also be damped, however, the resistance reduces the high frequency harmonic attenuation capability of LC filter.

Figure 2.6 (c) shows the passive damping method for the resistor in series with the capacitor whose damping characteristic is similar to **Figure 2.6 (a)**. **Figure 2.6 (d)** shows the passive damping method for the resistor in parallel with capacitor whose damping characteristic is similar to **Figure 2.6 (b)**. So, if the energy consumption is not considered, the damping resistor in series with inductor or in parallel with capacitor is a better choice.

2.6 Parameters design

The following is the parameters design process for passive damping method.

1. Resistor R_{L1} in series with Inductor L

$$R_{L1} > kp \cdot k_{PWM} \cdot \omega_r \cdot L \quad (2.18)$$

2. Resistor R_{L2} in parallel with Inductor L

$$R_{L2} < \frac{\sqrt{1 - (kp \cdot k_{PWM})^2}}{kp \cdot k_{PWM} \cdot \omega_r \cdot C} \quad (2.19)$$

3. Resistor R_{C1} in series with Inductor C

$$R_{C1} > \frac{kp \cdot k_{PWM} \cdot \omega_r \cdot L}{\sqrt{1 - (kp \cdot k_{PWM})^2}} \quad (2.20)$$

4. Resistor R_{C2} in parallel with Inductor C

$$R_{C2} < \frac{1}{kp \cdot k_{PWM} \cdot \omega_r \cdot C} \quad (2.21)$$

2.7 Simulation and results

To verify the correctness of the previous analysis and the effectiveness of the proposed parameter design method, the simulation model of the LC type single phase off grid inverter is carried out on PSIM. The parameters of the off-grid inverter and control loop are shown in **Table 2-2**

Table 2-2 Parameters of the off-grid inverter and control parameters

Parameter	Case I	Case II	Case III	Case IV
Inductor L	0.5 mH	1.0 mH	1.0 mH	1.0 mH
Capacitor C	10 μ F	50 μ F	50 μ F	50 μ F
Resonance frequency f_r	2251 Hz	712 Hz	712 Hz	712 Hz
DC-side voltage U_{dc}	80 V			
Output voltage U_o (RMS)	50 V			
The gain K_{PWM}	1			
Sampling frequency f_s	5 kHz			
Voltage regular proportional gain k_p	0.015	0.000015	0.015	0.015
Voltage regular resonance gain k_r	20			
Damping resistor R	0	0	2 Ω	

Figure 2.7 and **Figure 2.8** show the output voltage waveform of the inverter

when $f_r > f_s/3$. It can be seen that the system is stable. However, the total harmonics distortion is 3.52% which cannot meet the requirements.

Figure 2.9 shows the output voltage waveform of inverter without passive damping when $f_r < f_s/3$. The result shows the system cannot be stable which is the same as our analysis.

Figure 2.10 and **Figure 2.11** show the output voltage waveform and spectrum of the inverter with a damping resistor in series with inductor when $f_r < f_s/3$. By using the damping resistor, the Oscillation is damped effectively and the total harmonic distortion is 0.261%.

Figure 2.12 and **Figure 2.13** show the output voltage waveform and spectrum of the inverter with a damping resistor in parallel with inductor when $f_r < f_s/3$. The result shows the system still can be stable. However, the THD increases significantly compared with **Figure 2.11** and the harmonics of output voltage with UDF-SPWM are mainly at twice the switching frequency, which confirms the analysis.

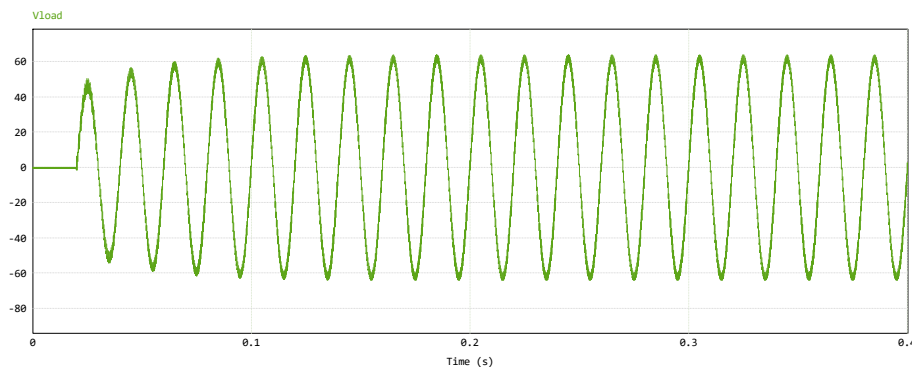


Figure 2.7 Output voltage waveform of Case I simulation model

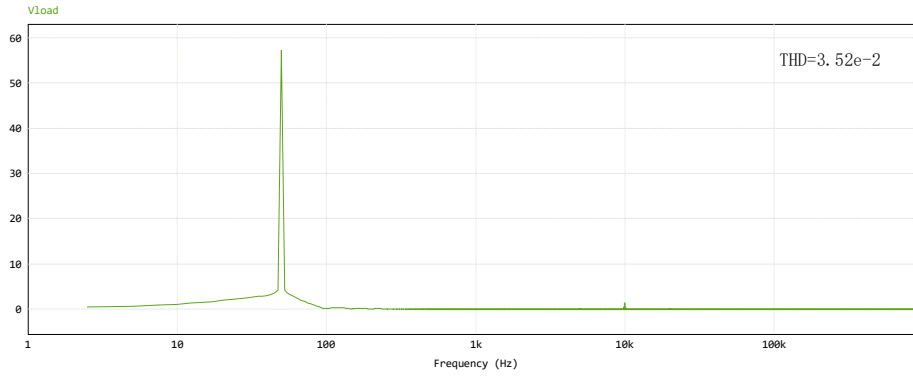


Figure 2.8 Output voltage spectrum of Case I simulation model

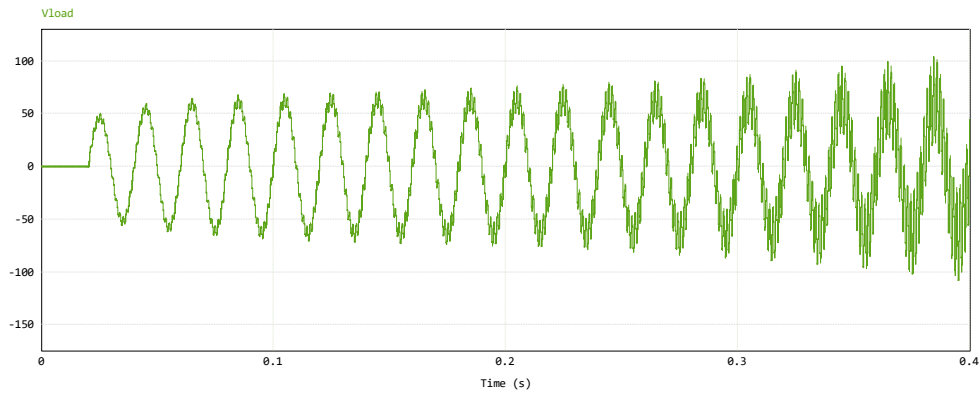


Figure 2.9 Output voltage waveform of Case II simulation model

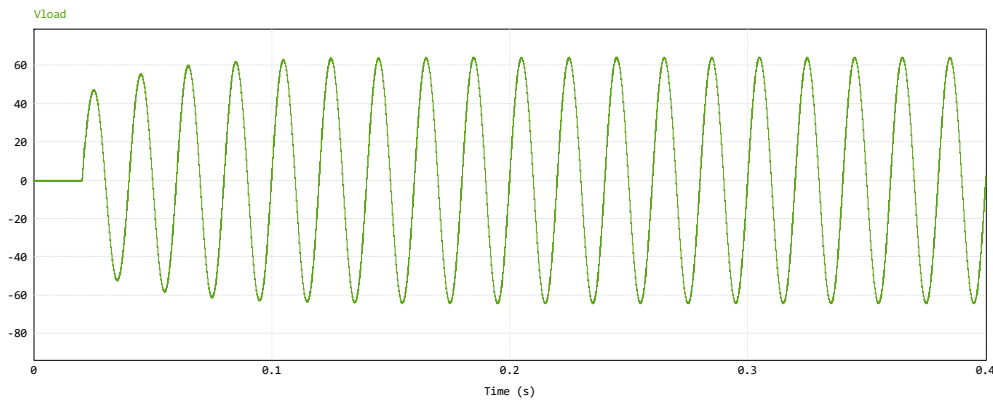


Figure 2.10 Output voltage waveform of Case III simulation model

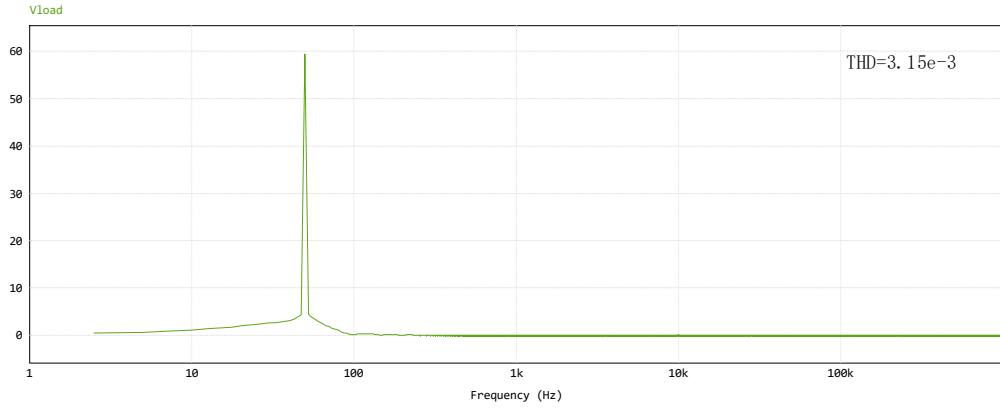


Figure 2.11 Output voltage spectrum of Case III simulation model

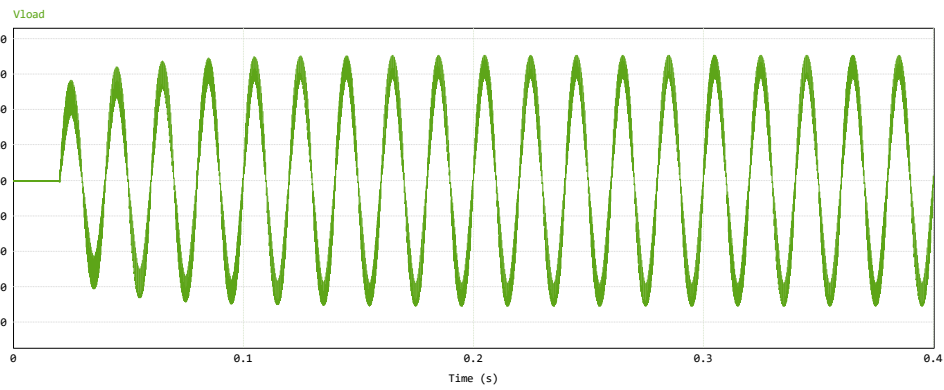


Figure 2.12 Output voltage waveform of Case IV simulation model

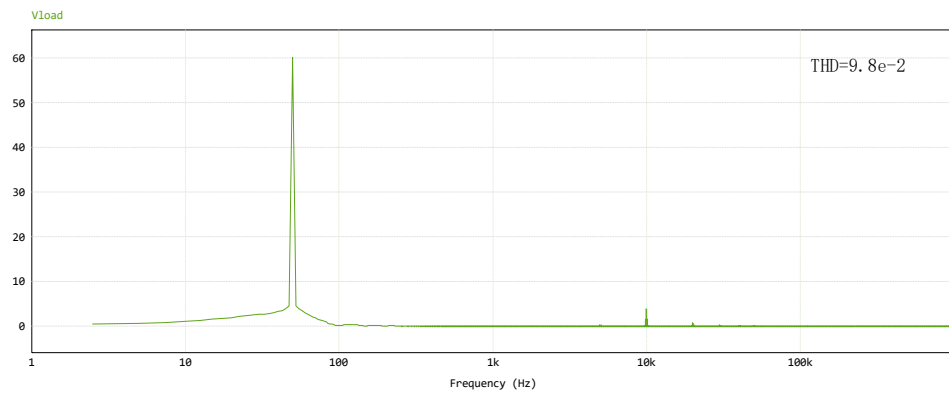


Figure 2.13 Output voltage spectrum of Case IV simulation model

2.8 Conclusion

In this chapter, the open loop transfer function of the inverter with single voltage loop control is derived from the forementioned mathematic model. According to the

stability analysis, the system with $kp < \left|1 - LC(2\pi f_s / 3)^2\right| / K_{PWM}$ can be stable when $f_r > f_s / 3$ and the system cannot be stable even with small kp when $f_r < f_s / 3$ due to the resonance peak. Although the system with appropriate control parameters can be stabilized when $f_r > f_s / 3$, the THD cannot satisfy the requirement. Therefore, passive damping approaches are proposed which can stabilize the system when $f_r < f_s / 3$. The simulation results confirm the effectiveness of the proposed approach. However, the passive damping method has a huge drawback which is energy consumption. Accordingly, it is necessary to investigate other methods to keep the system stable when $f_r < f_s / 3$.

Chapter 3 Stability Analysis of the Inverter with Inductor-Current Feedback Active Damping

3.1 Introduction

Compared with passive damping methods, active damping methods do not consume energy. [10] investigated the stability of the LC-type off-grid inverters with inductor-current feedback active damping when resonance frequency changes from 0 to $f_s/4$. [20] further studied the stability of the same system when f_r is extended to $f_s/3$. Since my study is based on their previous work, this chapter will discuss their research and experiment to prepare the knowledge for introducing my study that will be covered later.

3.2 Model of the inverter with Inductor-Current Feedback

Figure 3.1 shows the topology of the LC type off-grid inverter with inductor-current feedback active damping. Compared with **Figure 2.1**, there is an inner inductor current control loop adopted as the feedback, with H as the damping coefficient.

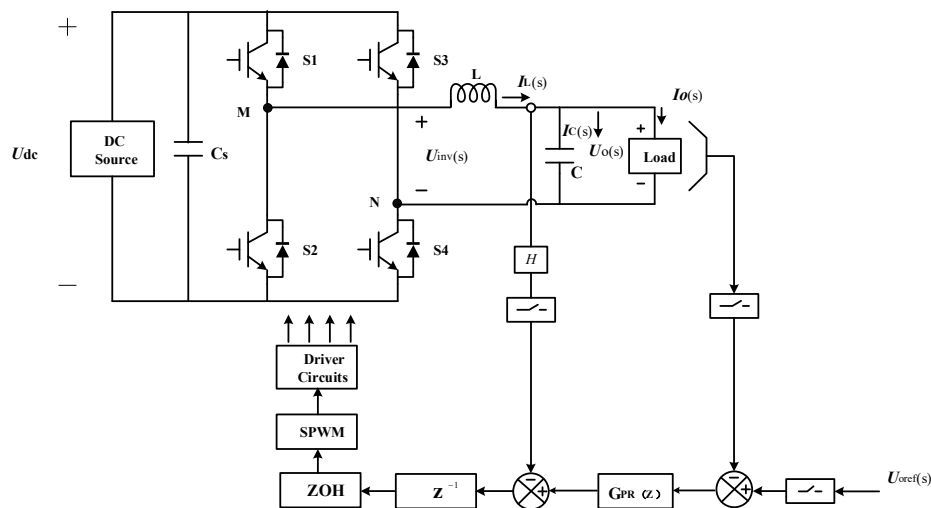


Figure 3.1 Topology of the LC type inverter with inductor-current feedback

Figure 3.2 and **Figure 3.3** show the control scheme of the LC-type off-grid inverter with inductor-current feedback active damping hybrid domain model and s domain model based on **Figure 3.1**. The load has been neglected for stability analysis in both models.

According to **Figure 3.3 (b)**, it can be found that the inner inductor current loop control can be modified to the virtual impedance Z_{eq} which is in series with the inductor L . The virtual impedance can be expressed by

$$Z_{eq} = HK_{PWM} e^{-1.5sT_s} \quad (3.1)$$

To investigate the physical meaning of virtual impedance, it can be given in complex form by applying Euler's formula

$$Z_{eq} = HK_{PWM} \cos(1.5\omega T_s) - jHK_{PWM} \sin(1.5\omega T_s) \quad (3.2)$$

When the real part of the virtual impedance is positive, the resonance peak can be damped, which is similar to passive damping method. This is the reason why the system can become stable when implementing the active damping method. According to (3.2), imaginary part can affect the actual resonance frequency f_r' . Specifically, the actual resonance frequency f_r' is greater than the resonance frequency f_r when $HK_{PWM} \sin(1.5\omega T_s)$ is positive and the actual resonance frequency f_r' is smaller than the resonance frequency f_r when $HK_{PWM} \sin(1.5\omega T_s)$ is negative.

$G_{iL}(s)$ is the transfer function from the inverter output voltage to inductor current, which can be given by

$$G_{iL}(s) = \frac{1}{sL} \cdot \frac{s^2}{s^2 + \omega_r^2} \quad (3.3)$$

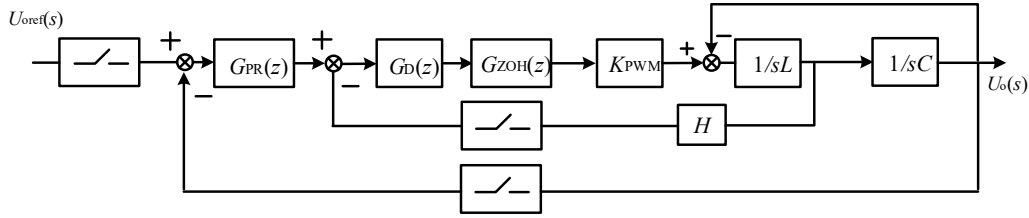
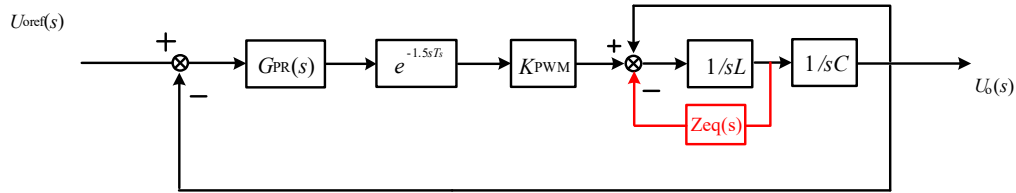
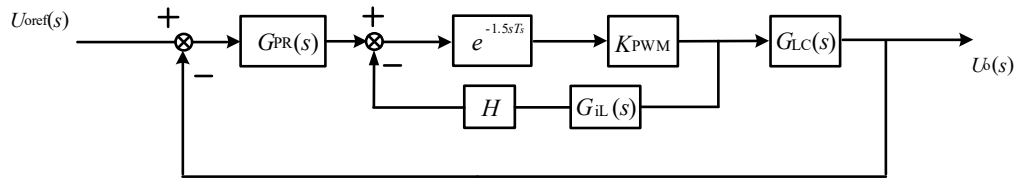


Figure 3.2 Control scheme of the inverter with inductor-current feedback in hybrid domain



(a) Equivalent control scheme 1



(b) Equivalent control scheme 2

Figure 3.3 Equivalent control scheme of the LC-type off-grid inverter with inductor-current feedback in s domain

According to **Figure 3.3**, the continuous version of open loop transfer function can be expressed by

$$T_{os}(s) = \frac{K_{PWM} G_{PR}(s) e^{-1.5sT_s}}{LCs^2 + HCK_{PWM} e^{-1.5sT_s} s + 1} \quad (3.4)$$

Since the s domain model is not convenient for calculation, z domain model is built which is shown in **Figure 3.4**. $G_{iL}(z)$ and $G_{LC}(z)$ are the z domain models of $G_{iL}(s)$ and $G_{LC}(s)$ with ZOH discretization method

$$G_{iL}(z) = \frac{\sin(\omega_r T_s)}{\omega_r L} \cdot \frac{z-1}{z^2 - 2z \cos(\omega_r T_s) + 1} \quad (3.5)$$

$$G_{LC}(z) = (1 - \cos(\omega_r T_s)) \cdot \frac{z+1}{z^2 - 2z \cos(\omega_r T_s) + 1} \quad (3.6)$$

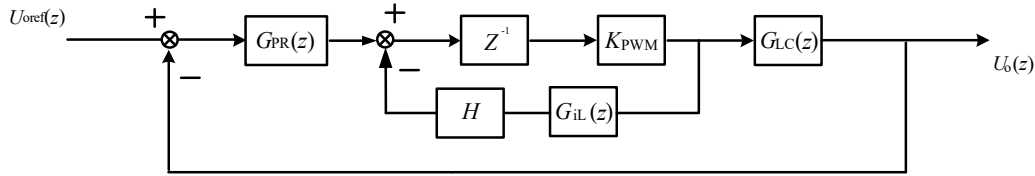


Figure 3.4 Equivalent control scheme of the LC-type off-grid inverter with inductor-current feedback in z domain

Consequently, the discrete model of the open loop transfer function can be calculated as

$$T_{oz}(z) = \frac{K_{PWM} G_{PR}(z)(1 - \cos(\omega_r T_s))(1+z)}{z(z^2 - 2z \cos(\omega_r T_s) + 1) + K_{PWM} \frac{H \sin(\omega_r T_s)}{\omega_r L} (z-1)} \quad (3.7)$$

3.3 Stability analysis

As mentioned earlier, when doing stability analysis, the first step is to investigate the distribution of the poles of the open loop transfer function $T_{oz}(z)$. The denominator of $T_{oz}(z)$ is shown below

$$Den(z) = z(z^2 - 2z \cos(\omega_r T_s) + 1) + K_{PWM} \frac{H \sin(\omega_r T_s)}{\omega_r L} (z-1) = 0 \quad (3.8)$$

$$Z = \frac{1+w}{1-w} \quad (3.9)$$

$$Den(w) = a_0 w^3 + a_1 w^2 + a_2 w + a_3 \quad (3.10)$$

(3-10) is obtained by substituting (3.9) into (3.8), where

$$\left\{ \begin{array}{l} a_0 = 1 + \cos(\omega_r T_s) + \frac{HK_{PWM} \sin(\omega_r T_s)}{\omega_r L} \\ a_1 = 1 + \cos(\omega_r T_s) - \frac{2HK_{PWM} \sin(\omega_r T_s)}{\omega_r L} \\ a_2 = 1 - \cos(\omega_r T_s) + \frac{HK_{PWM} \sin(\omega_r T_s)}{\omega_r L} \\ a_3 = 1 - \cos(\omega_r T_s) \end{array} \right. \quad (3.11)$$

$$\begin{array}{ccc} w^3 & a_0 & a_2 \\ w^2 & a_1 & a_3 \\ w^1 & b_1 & 0 \\ w^0 & a_3 & \end{array} \quad (3.12)$$

(3.12) is the Routh array, where

$$b_1 = (a_1 a_2 - a_0 a_3) / a_1 \quad (3.13)$$

According to Routh–Hurwitz stability criterion, the number of sign changes in the first column will be the number of the unstable poles of $Den(z)$. Since the damping coefficient H can affect the number of sign changes in the first column, the threshold needs to be calculated. H_{cirt1} is the threshold when a_0 equals zero; H_{cirt2} is the threshold when a_1 equals zero; H_{cirt3} and H_{cirt4} are the threshold when b_1 equals zero, which are shown as follows.

$$H_{cirt1} = -\frac{(1 + \cos(\omega_r T_s))\omega_r L}{K_{PWM} \sin(\omega_r T_s)} \quad (3.14)$$

$$H_{cirt2} = \frac{(1 + \cos(\omega_r T_s))\omega_r L}{2K_{PWM} \sin(\omega_r T_s)} \quad (3.15)$$

$$H_{cirt3} = \frac{(-1 + 2 \cos(\omega_r T_s))\omega_r L}{K_{PWM} \sin(\omega_r T_s)} \quad (3.16)$$

$$H_{cirt4} = 0 \quad (3.17)$$

According to [20], there are 3 stable cases which are shown in **Table 3-1**

Table 3-1 Unstable poles of the open loop transfer function

Case	f_r	H	Unstable Poles
1	$f_r < f_s / 6$	$0 < H < H_{cirt3}$	0
2	$f_s / 6 < f_r < f_s / 4$	$H_{cirt3} < H < 0$	0
3	$f_s / 4 < f_r < f_s / 3$	$H_{cirt1} < H < 0$	0

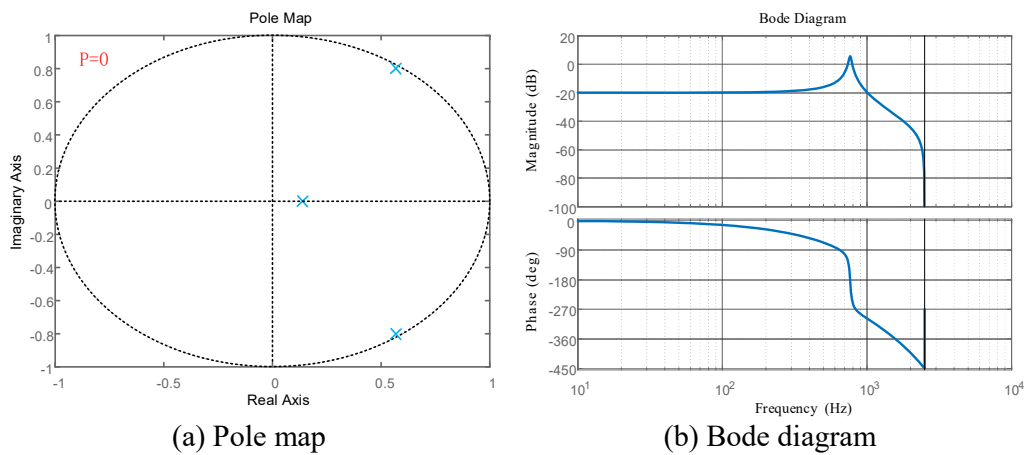


Figure 3.5 Pole map and the bode diagram of case 1

Case 1: According to **Table 3-1**, there is no positive pole of open loop transfer function. Correspondingly, the system can be stable if and only if $(N^+ - N^-)$ equals zero. As it can be seen in **Figure 3.5**, there is no positive crossing and one negative crossing which happens at f_r' . Therefore, with Small k_p , the magnitude of $T_{oz}(z)$ can be below unit at f_r' , which can void the negative crossing. Finally, $Z=0$ and thus the system can be stable.

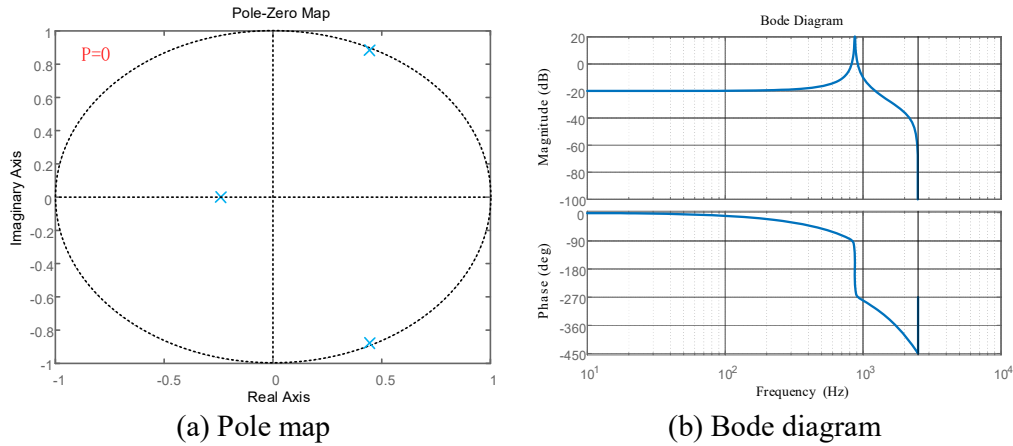


Figure 3.6 Pole map and the bode diagram of case 2

Case 2: According to **Table 3-1**, there is no positive pole of open loop transfer function. Correspondingly, the system can be stable if and only if $(N^+ - N^-)$ equals zero. As it can be seen in **Figure 3.6**, there is no positive crossing and one negative crossing which happens at f_r' . Therefore, with Small k_p , the magnitude of $T_{oz}(z)$ can be below unit at f_r' , which can void the negative crossing. Finally, $Z=0$ and thus the system can be stable.

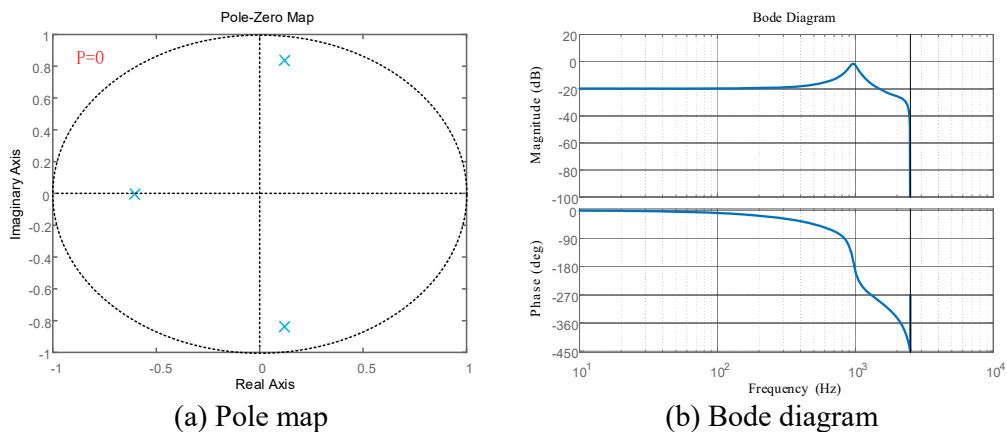


Figure 3.7 Pole map and the bode diagram of case 3

Case 3: According to **Table 3-1**, there is no positive pole of open loop transfer function. correspondingly, the system can be stable if and only if $(N^+ - N^-)$ equals zero.

As it can be seen in **Figure 3.7**, there is no positive crossing and one negative crossing which happens at f_r' . Therefore, with Small k_p , the magnitude of $T_{oz}(z)$ can be below unit at f_r' , which can void the negative crossing. Finally, $Z=0$ and thus the system can be stable.

3.4 Parameters design method

Based on previous analysis, the open loop transfer function has no unstable poles and positive crossing in the above 3 cases, which means P and N^+ both equal zero. To satisfy the conditions of stability, N^- should equal zero. This can be done by selecting appropriate k_p to limit the magnitude of $T_{oz}(z)$ at actual resonance frequency f_r' below unit.

Table 3-2 Parameters of the off-grid inverter

Parameter	Case A	Case B	Case C
Inductor L	1.3 mH		
Capacitor C	40 μF	20 μF	10 μF
Resonance frequency f_r	698Hz	987 Hz	1396Hz
DC-side voltage U_{dc}	80 V		
Output voltage U_o	50 V		
The gain K_{PWM}	1		
Sampling frequency f_s	5kHz		

Table 3-2 shows the three different cases with parameters. According to the parameter tuning method of coefficient of inductor-current feedback AD which has been mentioned in [10], the proportional gain k_p and optimal damping coefficient H can be attained in **Figure 3.8**. The resonance gain k_r can be determined based on the steady-state error. **Table 3-3** shows the final control parameters.

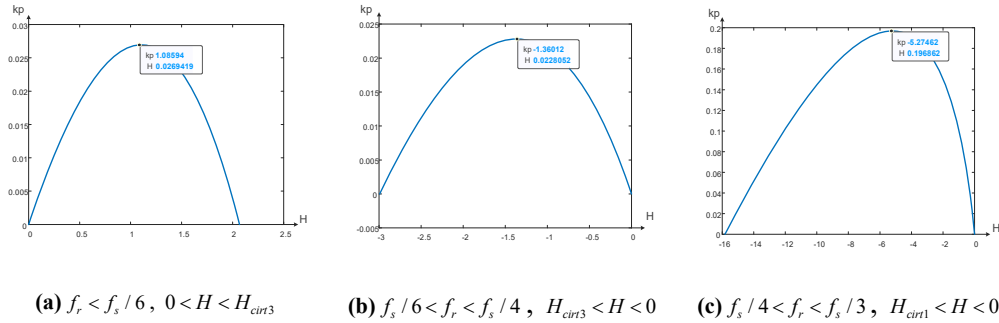


Figure 3.8 Value of k_{max} with the change of H

Table 3-3 Control Parameters

Parameter	Case A	Case B	Case C
kp	0.015	0.015	0.15
kr	20	20	20
H	1.08	-1.36	-5.27

3.5 Simulation and results

To verify the correctness of the previous analysis and the effectiveness of the proposed parameter design method, the simulation model of the LC type single phase off grid inverter is carried out on PSIM. The experimental parameters are shown in **Table 3-2** and **Table 3-3**.

Figure 3.9 and **Figure 3.10** show the output waveforms of the inverter and the voltage spectrum with $f_r < f_s / 6$ and $0 < H < H_{cirt3}$. The result shows the system can be stabilized without load and the total harmonic distortion is 0.28%. Turn on the load at 0.2s and it can be observed that there is a slight decrease in voltage, however, it quickly returns to steady state.

Figure 3.11 and **Figure 3.12** show the output waveforms of inverter and the voltage spectrum with $f_s / 4 < f_r < f_s / 3$ and $H_{cirt3} < H < 0$. The result shows the system can be stabilized without load and the total harmonic distortion is 0.56%. Compared with case A, the harmonics suppression capability is decreased. This is

because the resonance frequency of case B is greater than that of case A. Turn on the load at 0.2s and there is a slight increase in voltage, however, it quickly returns to steady state.

Figure 3.13 and **Figure 3.14** show the output waveforms of inverter and the voltage spectrum with $f_s/6 < f_r < f_s/4$ and $H_{cirt1} < H < 0$. The result shows the system can be stabilized without load and the total harmonic distortion is 1.12%. Compared with case A and case B, the harmonics suppression capability is worse. The reason is the same as mentioned above. Turn on the load at 0.2s and the increase in voltage is greater than that of case B, however, it still can return to steady state.

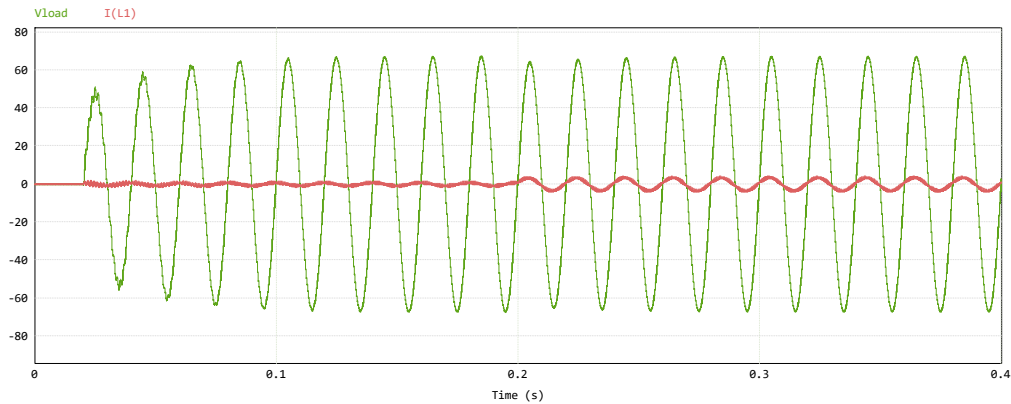


Figure 3.9 Output voltage and load current waveforms of Case A

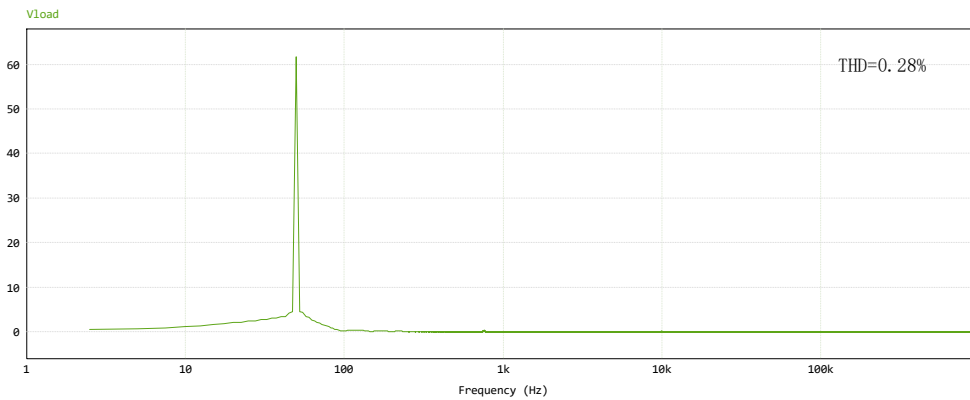


Figure 3.10 Output voltage spectrum of Case A

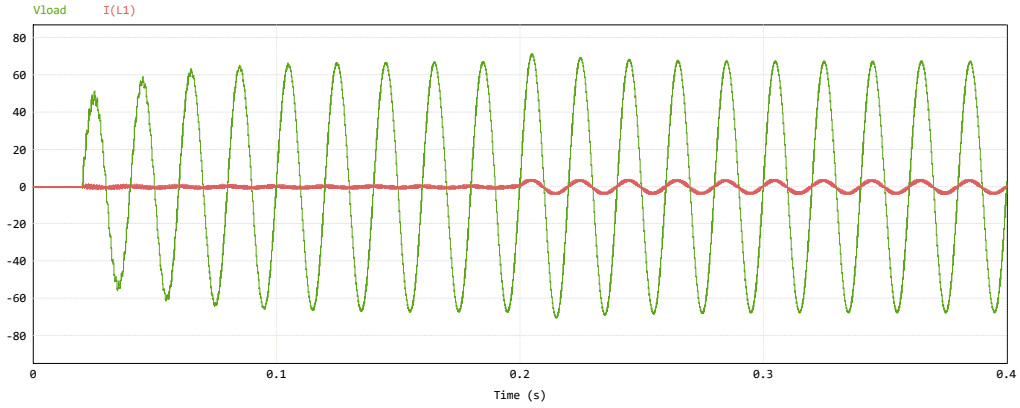


Figure 3.11 Output voltage and load current waveforms of Case B

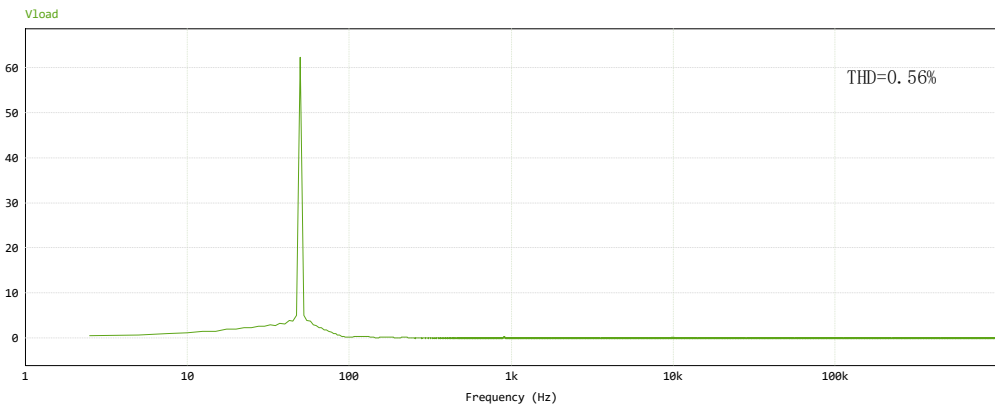


Figure 3.12 Output voltage spectrum of Case B

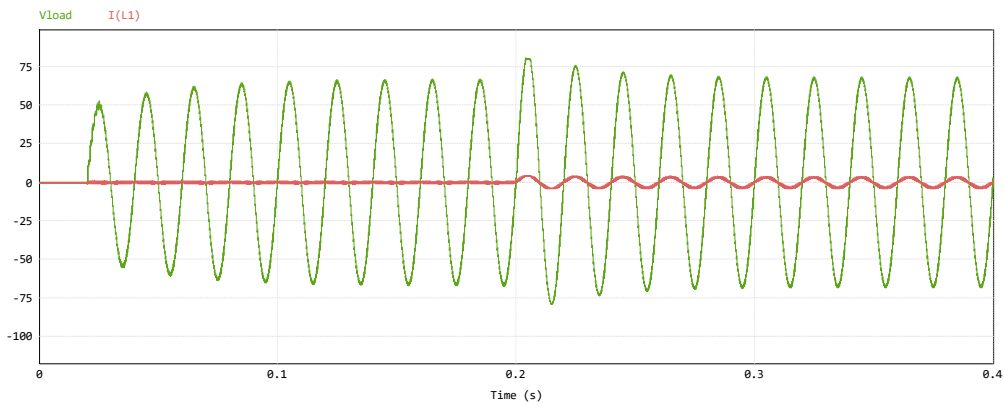


Figure 3.13 Output voltage and load current waveforms of Case C

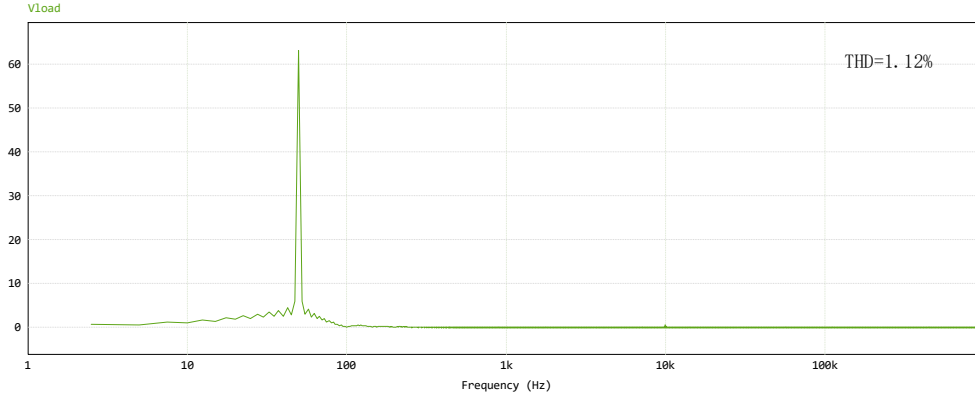


Figure 3.14 Output voltage spectrum of Case C

3.6 Conclusion

In this chapter, the open loop transfer function of the inverter with inductor current feedback active damping has been derived from the forementioned mathematical model. According to the previous stability analysis, there are three feasible combinations of one precondition (i.e., resonance frequency) and two determined stable conditions, each of which can stabilize the system, listed as follows:

$$(1) \quad 0 < f_r < f_s / 6, \quad 0 < H < H_{cirt3}, \quad |T_{oz}(j\omega_r')| < 1$$

$$(2) \quad f_s / 6 < f_r < f_s / 4, \quad H_{cirt3} < H < 0, \quad |T_{oz}(j\omega_r')| < 1$$

$$(3) \quad f_s / 4 < f_r < f_s / 3, \quad H_{cirt1} < H < 0, \quad |T_{oz}(j\omega_r')| < 1$$

the optimal feedback coefficient H and maximum proportional gain k_p can be attained with the proposed parameters design method. The simulation results confirm the correctness of the analysis and effectiveness of the proposed approach.

To fulfill the requirements of THD, the first combination is frequently chosen. However, f_r has the potential to be greater than $f_s / 6$ (the precondition of the second combination) in practical applications due to the production process, temperature, component aging, core saturation and other factors[19]. If that happens and the two

determined stable conditions are kept the same, the system will become unstable, for the system can only stay stable with the both determined stable conditions sticking to its original precondition (resonance frequency). What's more, [10] also mentioned that if the f_r close to $f_s / 6$ even without crossing the boundary of the original precondition, the system cannot be stable. Therefore, we need to extend the effective damping region.

Chapter 4 A Lag Compensation Method Based on All-Pass Filter

4.1 Introduction

[10] mentioned, when f_r is close to $f_s/6$, the inverter with inductor-current feedback active damping cannot be stable. However, it did not give strict mathematical proof. To explain why the system cannot be stable when f_r is close to $f_s/6$, the mathematical derivation in z domain is given in this chapter. Then a lag compensation method is proposed to deal with this problem. Finally, the simulation results confirm the effectiveness of the proposed approach.

4.2 Stability analysis

The model used in this chapter is the same as that in chapter 3. The open loop transfer function can be shown as

$$T_{oz}(z) = \frac{K_{PWM} G_{PR}(z)(1 - \cos(\omega_r T_s))(1 + z)}{z(z^2 - 2z\cos(\omega_r T_s) + 1) + K_{PWM} \frac{H \sin(\omega_r T_s)}{\omega_r L} (z-1)} \quad (4.1)$$

4.2.1 Number of unstable poles

To investigate the stability of $T_{oz}(z)$ when resonance frequency equals $f_s/6$, it is necessary to analyze the number of the unstable poles of the open-loop transfer function, and thus the denominator of $T_{oz}(z)$ can be extracted as

$$Den(z) = z(z^2 - 2z\cos(\omega_r T_s) + 1) + K_{PWM} \frac{H \sin(\omega_r T_s)}{\omega_r L} (z-1) = 0 \quad (4.2)$$

(4.3) is obtained by substituting (3.9) into (3.8), where

$$\begin{cases} a_0 = 1 + \cos(\omega_r T_s) + \frac{HK_{PWM} \sin(\omega_r T_s)}{\omega_r L} \\ a_1 = 1 + \cos(\omega_r T_s) - \frac{2HK_{PWM} \sin(\omega_r T_s)}{\omega_r L} \\ a_2 = 1 - \cos(\omega_r T_s) + \frac{HK_{PWM} \sin(\omega_r T_s)}{\omega_r L} \\ a_3 = 1 - \cos(\omega_r T_s) \end{cases} \quad (4.3)$$

$$\begin{array}{ccc} w^3 & a_0 & a_2 \\ w^2 & a_1 & a_3 \\ w^1 & b_1 & 0 \\ w^0 & a_3 & \end{array} \quad (4.4)$$

(4.4) is the Routh array, where

$$b_1 = (a_1 a_2 - a_0 a_3) / a_1 \quad (4.5)$$

As motioned in chapter 3, according to Routh–Hurwitz stability criterion, the number of sign changes in the first column will be the number of the positive roots of $Den(z)$. Since the damping coefficient H can affect the number of sign changes in the first column, the thresholds need to be calculated. Compared with chapter 3, when resonance frequency equals $f_s / 6$, the expression of H_{cirt1} , H_{cirt2} and H_{cirt4} are the same. The only difference is that H_{cirt3} equals zero.

Correspondingly, there are 4 different scenarios which are shown in **Table 4-1**

Table 4-1 The number of unstable poles

Scenario	f_r	H	poles
a	$f_r = f_s / 6$	$H < H_{cirt1}$	3
b		$H_{cirt1} < H < 0$	2
c		$0 < H < H_{cirt2}$	2
d		$H > H_{cirt2}$	2

4.2.2 -180° crossing

The unstable poles of open loop transfer function $T_{oz}(z)$ have been attained. Therefore, the next step is to investigate the bode diagram to examine whether it can meet the stable conditions. As mentioned in chapter 3, to simplify the analysis, assume K_{PWM} equals one and it can be found that $T_{oz}(z)$ is an imaginary number at $f_s/6$, which can be calculated as

$$T_{oz}(z = e^{j\pi/3}) = -j \frac{L\pi f_s k_p}{3H} \quad (4.8)$$

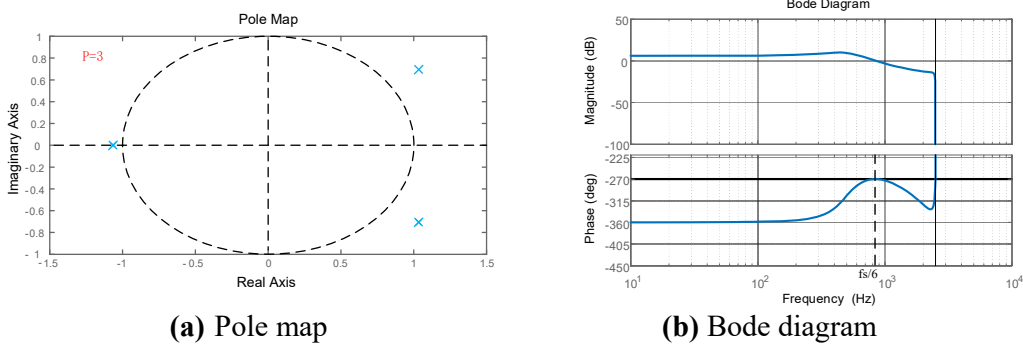


Figure 4.1 The pole map and the bode diagram of scenario a

Figure 4.1 shows the pole map and bode diagram of scenario a. According to **Figure 4.1(a)**, it can be observed that there are three unstable poles in scenario a. Thus, according to Nyquist stability criterion, the system can be stable if and only if $(N^+ - N^-)$ equals three. As seen in **Figure 4.1(b)**, there is no positive crossing and negative crossing, and k_p will not affect the phase, which means $(N^+ - N^-)$ equals zero. Therefore, $Z=3$ and the system cannot work stably.

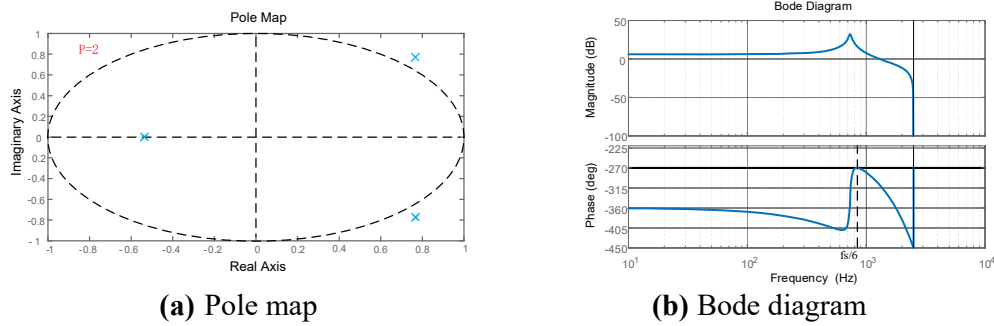


Figure 4.2 Pole map and the bode diagram of scenario b

Figure 4.2 shows the pole map and bode diagram of scenario b. According to **Figure 4.2 (a)**, it can be observed that there are two unstable poles in scenario b. Thus, according to Nyquist stability criterion, the system can be stable if and only if $(N^+ - N^-)$ equals two. As seen in **Figure 4.2 (b)**, there is no positive crossing and negative crossing, and k_p will not affect the phase, which means $(N^+ - N^-)$ equals zero. Therefore, $Z=2$ and the system cannot work stably.

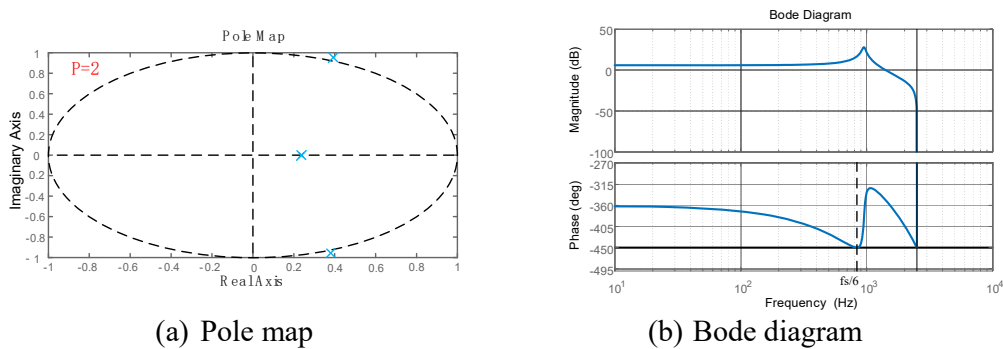
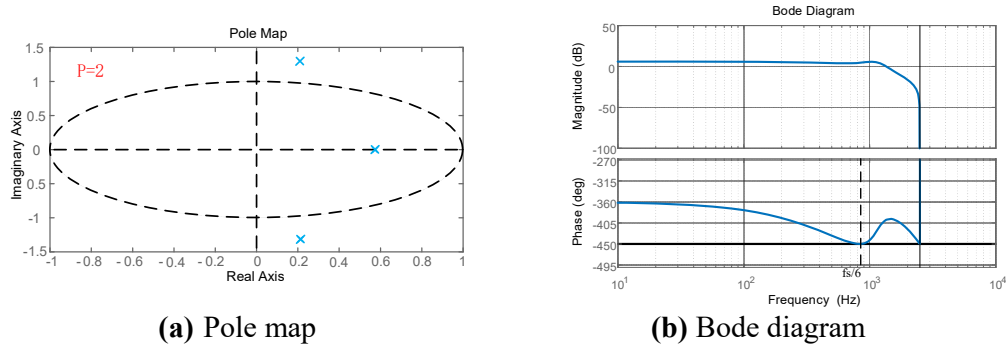


Figure 4.3 Pole map and the bode diagram of scenario c

Figure 4.3 shows the pole map and bode diagram of scenario c. According to **Figure 4.3 (a)**, it can be observed that there are two unstable poles in scenario c. Thus, according to Nyquist stability criterion, the system can be stable if and only if $(N^+ - N^-)$ equals two. As seen in **Figure 4.3 (b)**, there is no positive crossing and negative crossing,

and k_p will not affect the phase, which means $(N^+ - N^-)$ equals zero. Therefore, $Z=2$ and the system cannot work stably.



(a) Pole map

(b) Bode diagram

Figure 4.4 Pole map and the bode diagram of scenario d

Figure 4.4 shows the pole map and bode diagram of scenario d. According to **Figure 4.4 (a)**, it can be observed that there are two unstable poles in scenario d. Thus, according to Nyquist stability criterion, the system can be stable if and only if $(N^+ - N^-)$ equals two. As seen in **Figure 4.4 (b)**, there is no positive crossing and negative crossing, and k_p will not affect the phase, which means $(N^+ - N^-)$ equals zero. Therefore, $Z=2$ and the system cannot work stably.

Based on the analysis above, the system cannot be stabilized when resonance frequency equals $f_s / 6$. no matter how control parameters are selected.

In this chapter, scenario c is chosen to be analyzed. According to Nyquist stability criterion, if one positive crossing and zero negative crossing could be attained, the operation of the system has the potential to be stable. This can be realized by the lag compensation method in series with Q-PR controller, which has been shown in **Figure 4.5**. The ideal scheme is that the lag compensation method can provide the negative phase without affecting the magnitude and the amplitude of $T_{oz}(z)$ can be changed by

k_p , which can simplify the analysis.

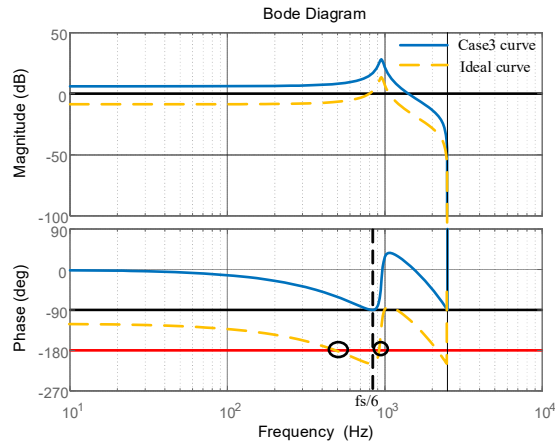
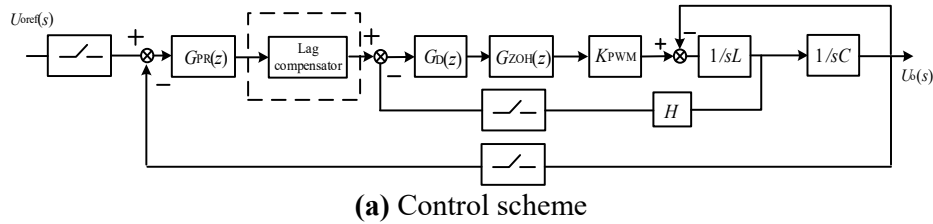


Figure 4.5 The ideal bode diagram

4.3 Lag compensation methods

4.3.1 Notch filter

Based on the previous analysis, Notch filter is proposed and its continuous version can be attained as [21]

$$G_n(s) = \frac{s^2 + \omega_n^2}{s^2 + Qs + \omega_n^2} \quad (4.9)$$

Where Q is the quality factor and ω_n is the notch frequency.

Figure 4.6 shows the bode diagram of the notch filter. In analog control, this kind of lag compensation method has a drawback. Because there is a negative peak and 180° phase jump at notch frequency. However, in digital control, the notch filter can be discretized with the first-order holder method and the notch frequency could be placed

at the frequency greater than Nyquist frequency, which means the negative peak and 180° phase jump can be avoided. This method has been applied to LCL-filter grid-connected inverter [21]. Nevertheless, the notch filter cannot be applied to LC-type off-grid inverter. This is because the maximum negative phase it can provide is -90° which cannot satisfy the requirement.

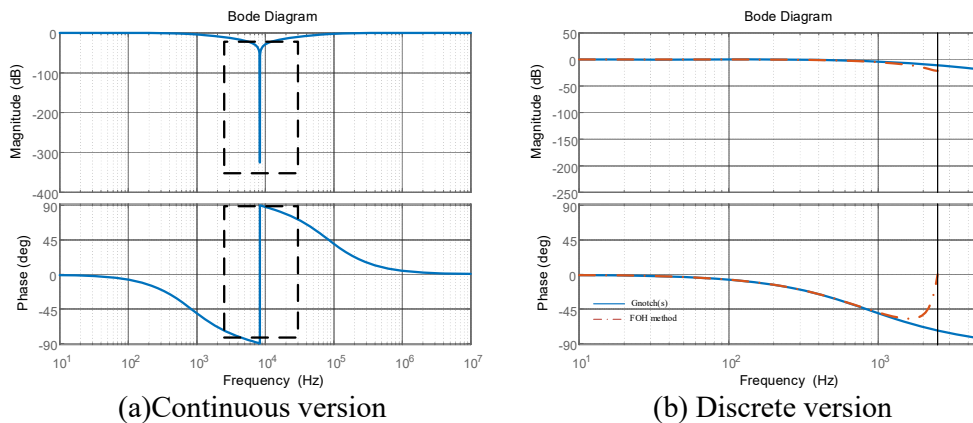


Figure 4.6 The bode diagram of Notch filter

4.3.2 All-pass filter

In this case, another method, all-pass filter, has been proposed [22] and it can be given as

$$G_p(z) = \frac{1-az}{z-a}, \quad 0 < a < 1 \quad (4.10)$$

Where a is the pole of the all-pass filter.

Figure 4.7 shows the bode diagram of all-pass filter with various poles a . As it can be observed that the magnitude of $G_p(z)$ in the entire frequency range is 0-dB and it can provide larger negative phase with pole a increased. Compared with notch filter, the maximum negative phase it can provide is -180° which can meet the requirement.

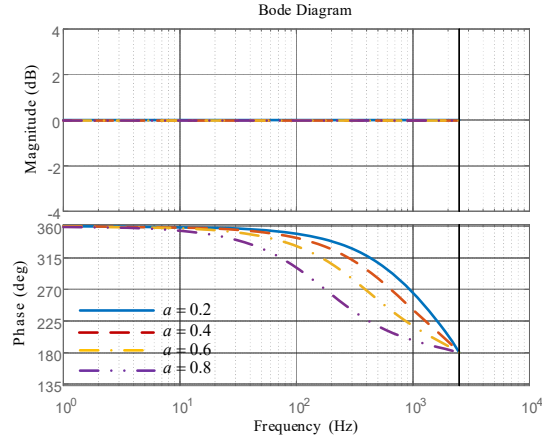


Figure 4.7 The bode diagram of all-pass filter

Accordingly, the pole a can be tuned to attain the required lagging phase at a certain frequency. In order to obtain the specific expression for the compensated phase of the all-pass filter, (4.10) can be converted into (4.11) by utilizing $z = e^{sT_s}$ and Euler's formula, which can be calculated as

$$G_c(\omega) = \frac{1 - a \cos(\omega T_s) - ja \sin(\omega T_s)}{\cos(\omega T_s) - a + j \sin(\omega T_s)} \quad (4.11)$$

Accordingly, the phase of all-pass filter can be attained from (4.11) as [22]

$$\varphi_c(\omega) = -\omega T_s - 2 \arctan \frac{a \sin(\omega T_s)}{1 - a \cos(\omega T_s)} \quad (4.12)$$

Based on the desired phase φ_{des} at specified frequency ω_{spec} , the pole a can be calculated as

$$a = \frac{\tan[0.5(\varphi_{des} + \omega_{spec} T)]}{\tan[0.5(\varphi_{des} + \omega_{spec} T)] \cos(\omega_{spec} T) - \sin(\omega_{spec} T)} \quad (4.13)$$

4.4 Parameters design

According to **Figure 4.5**, the specified frequency ω_{spec} is assumed to be $f_s / 6$. Considering the stable margin, the desired phase φ_{des} is assumed to be -110° . Based on

(4.13), the pole a can be calculated as 0.424. The bode diagram of the corresponding all-pass filter is shown in **Figure 4.8**, which confirms the analysis.

Figure 4.9 shows the bode diagram of open loop transfer function with all-pass filter when a equals 0.424. As it can be seen, there are one negative crossing at frequency $f1$ and one positive crossing at frequency $f2$. Furthermore, the magnitudes of T_{oz} at $f1$ and $f2$ are both greater than 0-dB, which means $N^- = N^+ = 1$.

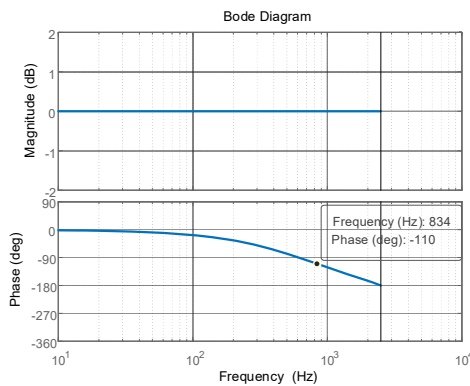


Figure 4.8 The bode diagram of all-pass filter with $a = 0.424$

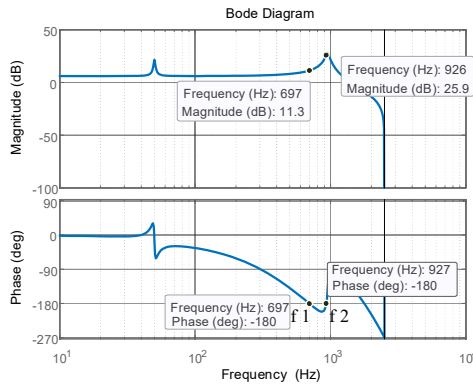


Figure 4.9 The bode diagram of scenario c with all-pass filter

Accordingly, the next step is to make the magnitude of T_{oz} at $f1$ smaller than 0-dB and make the magnitude of T_{oz} at $f2$ greater than 0-dB, which means $N^- = 0$ and $N^+ = 1$. This can be realized by equation (4.14), which can be shown as

$$\left| T_{oz} \left(z = e^{j\frac{\pi}{3}} \right) \right| = \left| \frac{k_p \pi f_s L}{j3H} \right| = 1 \quad (4.14)$$

k_p can be calculated as

$$k_p = \frac{3H}{\pi f_s L} \quad (4.15)$$

Figure 4.10 shows the final bode diagram of scenario c with all-pass filter, which perfectly demonstrates the prior analysis.

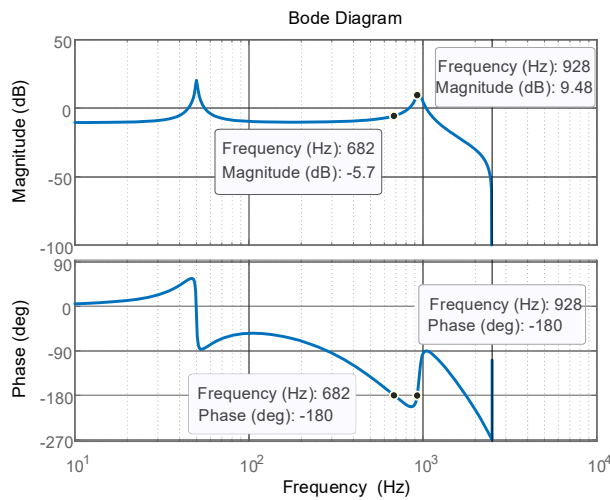


Figure 4.10 The final bode diagram of scenario c with all-pass filter

To investigate whether the system can still be stable when resonance frequency varies from $0.9f_s / 6$ to $1.1f_s / 6$, the closed loop transfer function $T_{co}(z)$ is explored, which can be shown as

$$T_{cz}(z) = \frac{T_{oz}(z)}{1 + T_{oz}(z)} \quad (4.16)$$

Figure 4.11 shows the pole of the overall system when resonance frequency f_r varies by 10% around $f_s / 6$. As it can be seen, the corresponding poles of closed loop transfer function are all in the unit circle, which means the system can be stable.

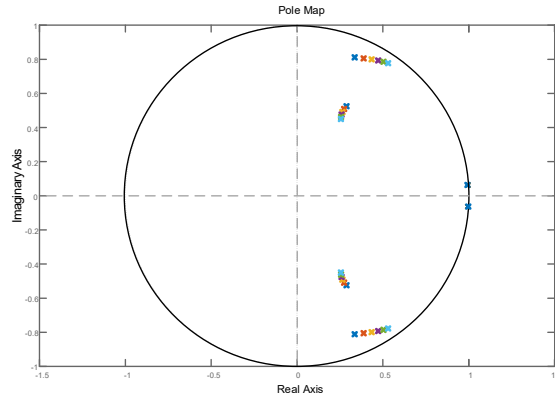


Figure 4.11 Pole map of the overall system when resonance frequency f_r are changed (changing from 90% of $f_s/6$ to 110% of $f_s/6$)

4.5 Design guideline

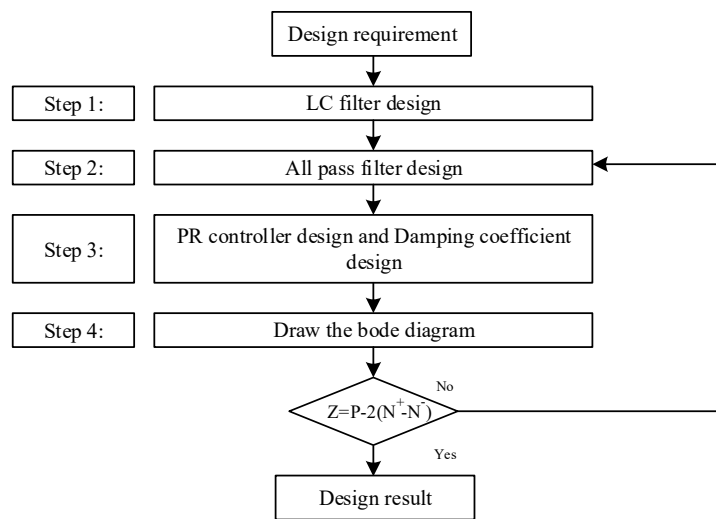


Figure 4.12 Design flowchart

Based on the analysis which has been mentioned above, the following step-by-step design approach is provided. **Figure 4.12** shows the Design flowchart.

Step 1: Considering the actual design factors such as power level, current limit, and resonant frequency, the inductance values L and capacitance values C are determined.

Step 2: Determine the parameters of the all-pass filter according to the phase angle

which needs to be compensated

Step 3: According to $0 < H < H_{crit2}$ and $k_p = 3H / \pi f_s L$, H and k_p can be determined.

Step 4: Draw the Bode diagram of the system and examine whether the stability conditions are satisfied. If not, come back to step 2 and restart the procedure.

4.6 Simulation

To verify the correctness of previous analysis and effectiveness of the proposed parameter design method, the simulation model of the LC-type single-phase off-grid inverter is carried out on PSIM. The experimental parameters are shown in **Table 4-2**.

Table 4-2 Parameters of the off-grid inverter and control parameters

Parameter	Case I	Case II	Case III
Inductor L	1.3 mH		
Capacitor C	34.5 μ F	28 μ F	23.2 μ F
Resonance frequency f_r	751Hz	834Hz	916Hz
DC-side voltage U_{dc}	80 V		
Output voltage U_o	50 V		
The gain K_{PWM}	1		
Sampling frequency f_s	5kHz		
Voltage regular proportional gain k_p	0.293		
Voltage regular resonance gain k_r	20		
Damping coefficient H	2		
a	0.424		

Figure 4.13 shows the output voltage waveform of the system without compensation. The simulation result shows the system cannot be stable, which is consistent with our analysis.

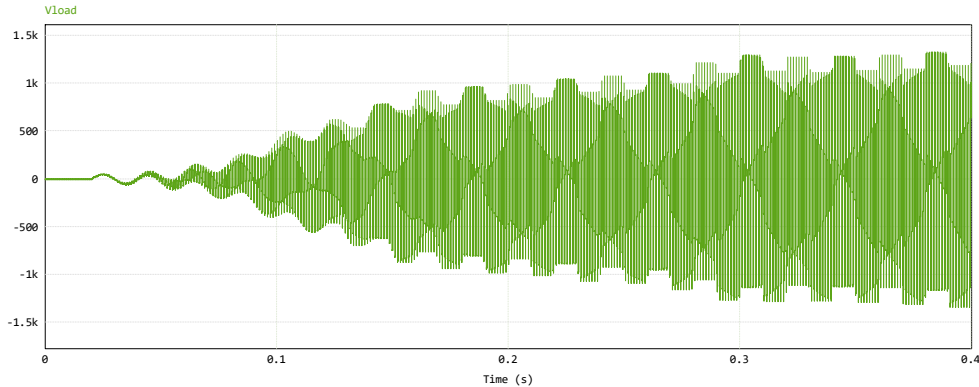


Figure 4.13 Output voltage waveform of the system without compensation

Figure 4.14 and **Figure 4.15** show the output waveforms of the inverter and the voltage spectrum when resonance frequency equals $0.9 f_s / 6$. As seen, the system can be stabilized with all-pass filter and the total harmonic distortion is 0.325%. Turn on the load at 0.2s and it can be observed that there is a slight decrease in voltage, however, it quickly returns to steady state.

Figure 4.16 and **Figure 4.17** show the output waveforms of the inverter and the voltage spectrum when resonance frequency equals $f_s / 6$. The result shows that the system can be stabilized with all-pass filter and the total harmonic distortion is 0.4%. Turn on the load at 0.2s and it can be noticed that the situation is the same with case I.

Figure 4.18 and **Figure 4.19** show the output waveforms of the inverter and the voltage spectrum when resonance frequency equals $1.1 * f_s / 6$. According to the simulation results, the system can be stabilized with all-pass filter and the total harmonic distortion is 0.478%. Turn on the load at 0.2s and there is still a slight decrease at 0.2s, however, it quickly returns to steady state.

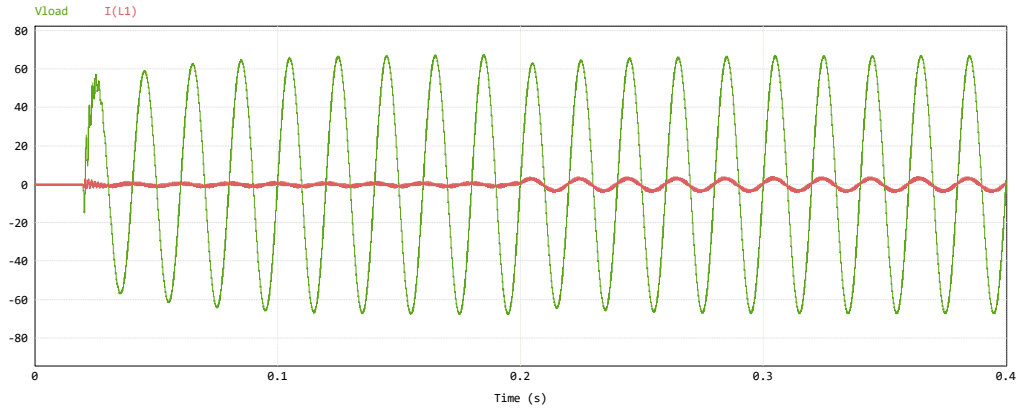


Figure 4.14 Output voltage and load current waveforms of Case I

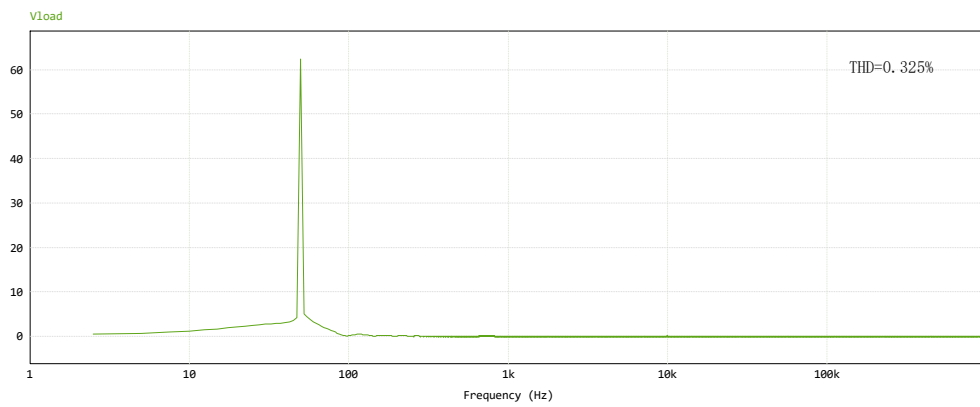


Figure 4.15 Output voltage spectrum of Case I

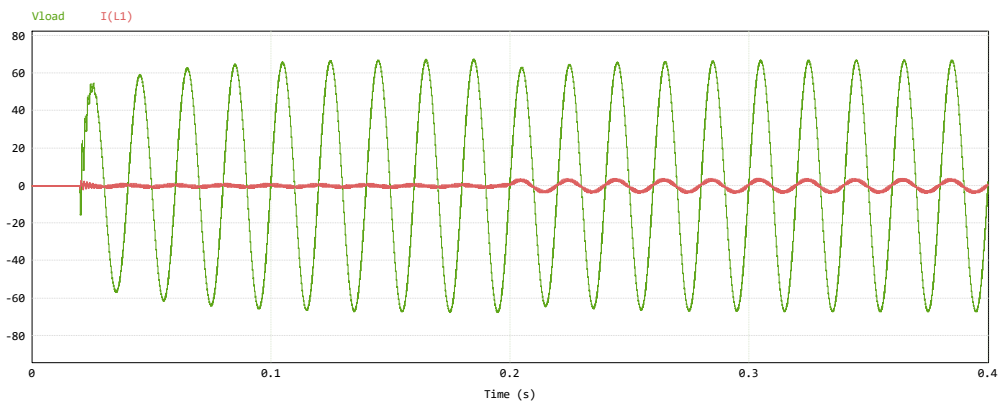


Figure 4.16 Output voltage and load current waveforms of Case II

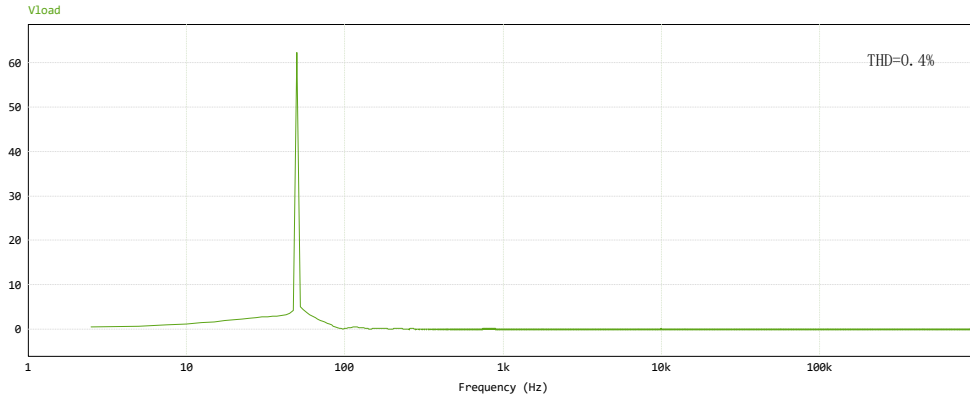


Figure 4.17 Output voltage spectrum of Case II

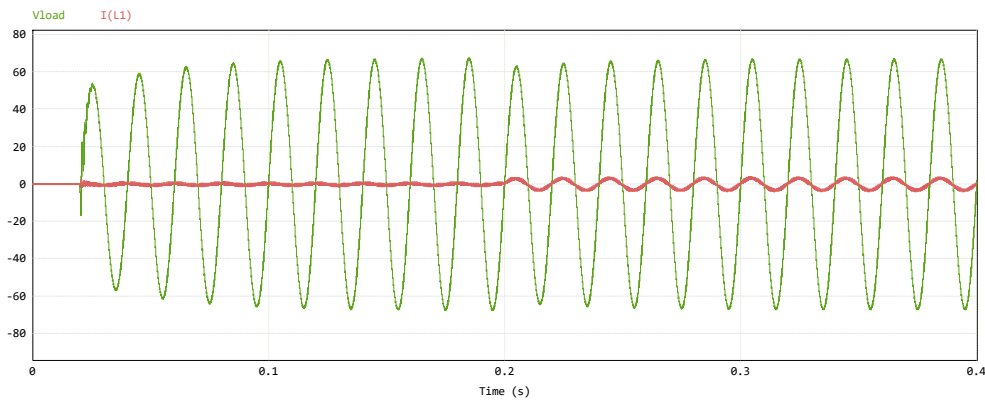


Figure 4.18 Output voltage and load current waveforms of Case III

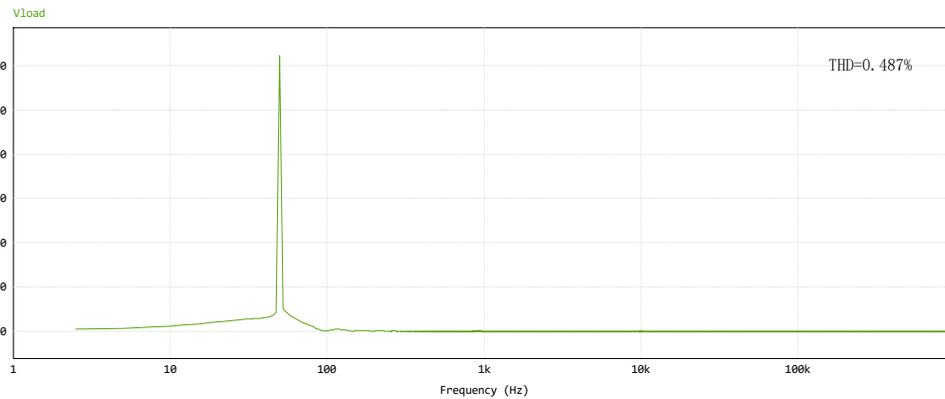


Figure 4.19 Output voltage spectrum of Case III

4.7 Conclusion

In this chapter, the strict mathematical derivation based on the open loop transfer function attended in chapter 3 is given to explain why the system is unstable when f_r

is equal to $f_s / 6$. What's more, the system still cannot be stable when f_r is close to $f_s / 6$. This is because when f_r approaches $f_s / 6$ positively, H is very small, which means the double loop control is equivalent to single loop control. According to chapter 2, the system with single voltage loop control cannot be stable when f_r smaller than $f_s / 3$. The system also cannot be stable with positive H when f_r approaches to $f_s / 6$ negatively. To fix this problem, a Lag compensation method based on all-pass filter and its corresponding design guideline are proposed. Finally, the simulation results confirm the effectiveness of the proposed approach. Nevertheless, as mentioned in the conclusion of chapter 3, there are many factors affecting resonance frequency. If the filter inductor works in a high temperature environment for a long time and the iron core of the filter inductor becomes saturated, the value of inductor will be reduced intensively, which could cause the resonant frequency to exceed the effective damping region. Therefore, we need to extend the stable region.

Chapter 5 A Lag Compensation Method Based on Negative First-Order Low-Pass Filter

5.1 Introduction

Traditional inductor-current feedback active damping can keep system stable when $0 < f_r < f_s/6$ and all-pass filter can stabilize the system when f_r is close to $f_s/6$. Considering the effective damping region is still narrow, an improved inductor-current feedback active damping based on Negative First-Order Low-Pass Filter is proposed. This approach can extend the effective damping region to f_c , where $f_c \in (f_s/3, f_s/2)$. Finally, the simulation results verify the effectiveness of this method.

5.2 Traditional inductor-current feedback active damping

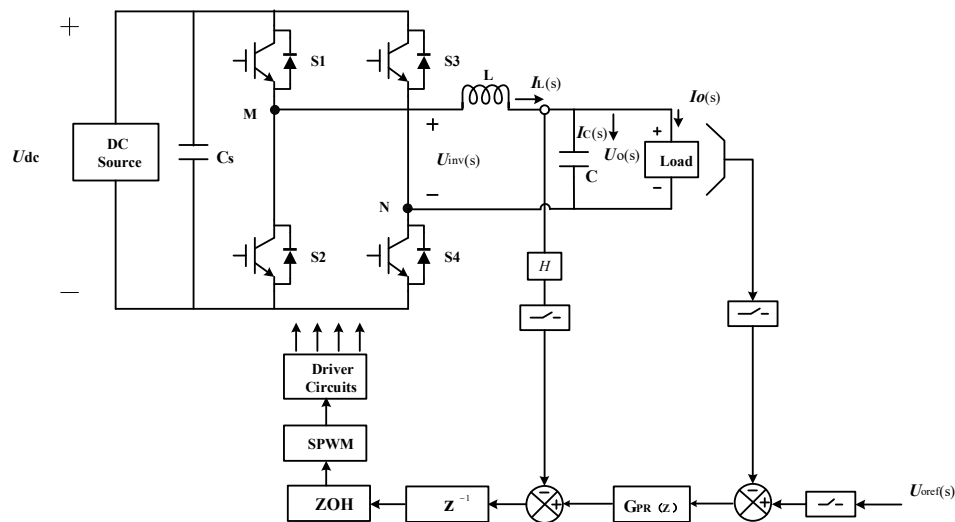


Figure 5.1 Topology of the inverter with traditional inductor-current feedback

Figure 5.1 shows the topology of the LC type inverter with traditional inductor-current feedback and the corresponding control scheme of hybrid domain model is shown in **Figure 5.2**. Based on **Figure 5.2**, the inner inductor current loop control can be modified to the virtual impedance Z_{eq} , which is shown in **Figure 5.3**. The transfer

function of the virtual impedance can be expressed by [10]

$$Z_{eq} = HK_{PWM} \cos(1.5\omega T_s) - jHK_{PWM} \sin(1.5\omega T_s) \quad (5.1)$$

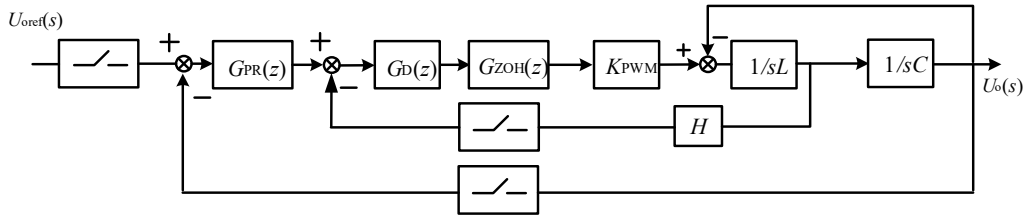


Figure 5.2 Control scheme of the inverter with traditional inductor-current feedback in hybrid domain

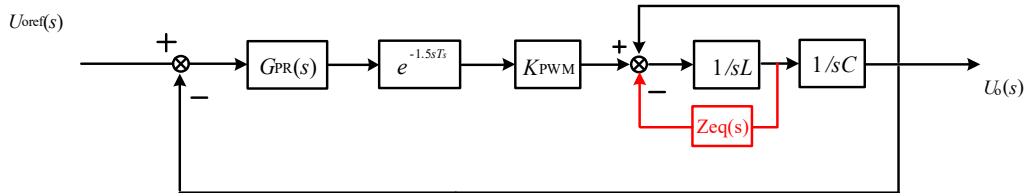


Figure 5.3 Equivalent control scheme of the LC-type off-grid inverter with traditional inductor-current feedback in s domain

According to (5.1), it can be observed that $R_{eq}(\omega) = HK_{PWM} \cos(1.5\omega T_s)$ and $X_{eq} = HK_{PWM} \sin(1.5\omega T_s)$. H is assumed to be positive and the frequency characteristic of R_{eq} and X_{eq} is shown in **Figure 5.4**, where the blue curve represents R_{eq} and the red curve represents X_{eq} .

As it can be noticed, only when $0 < f_r < f_s / 6$, R_{eq} is positive, when $f_s / 6 < f_r < f_s / 2$, R_{eq} is negative. Since negative virtual resistance produces unstable poles, the system cannot be stable when $f_s / 6 < f_r < f_s / 2$ [10].

Therefore, another method needs to be investigated to extend the region of positive virtual resistance.

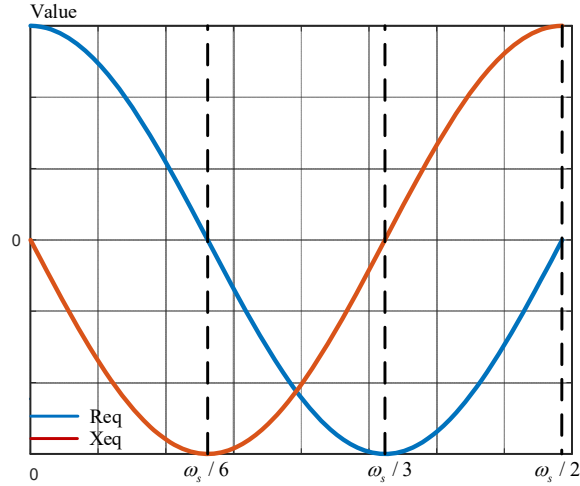


Figure 5.4 Characteristics of R_{eq} and X_{eq}

5.3 Improved capacitor-current feedback active damping with negative first-order low-pass filter

Figure 5.5 shows the Control scheme of the LC-type off-grid inverter with improved inductor-current feedback in hybrid domain. As it can be seen, the approach used to improve the system is to add a negative first-order low-pass filter, $G_f(s)$, into the inductor-current feedback branch. The transfer function of $G_f(s)$ can be expressed as [23]

$$G_f(s) = -\frac{1}{\lambda s + 1} \quad (5.2)$$

Where λ is the factor of negative first-order low-pass filter.

Similar to **Figure 5.3**, the inner inductor current loop control can also be altered to the virtual impedance Z_{eq2} , which is shown in

Figure 5.6. The transfer function of the new virtual impedance can be expressed by

$$Z_{eq2}(s) = HK_{PWM}G_f(s)e^{-1.5sT_s} \quad (5.3)$$

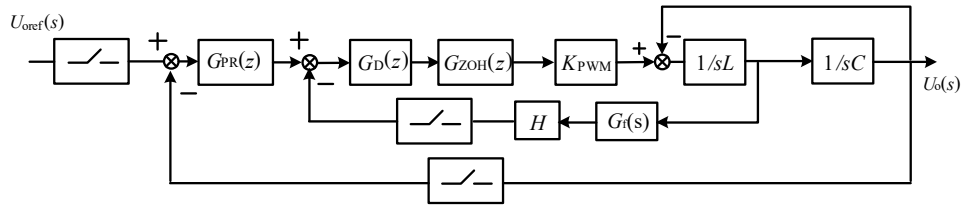


Figure 5.5 Control scheme of the inverter with improved inductor-current feedback in hybrid domain

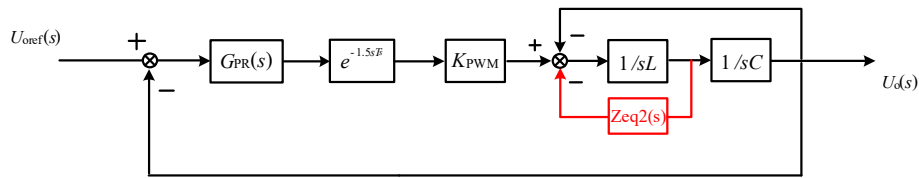


Figure 5.6 Control scheme of the inverter with improved inductor-current feedback in s domain

By applying Euler's formula to (5-3), R_{eq2} and X_{eq2} can be calculated as

$$R_{eq2}(\omega) = \frac{HK_{PWM}}{1 + \omega^2 \lambda^2} (\omega \lambda \sin 1.5\omega T_s - \cos 1.5\omega T_s) \quad (5.4)$$

$$X_{eq2}(\omega) = \frac{HK_{PWM}}{1 + \omega^2 \lambda^2} (\omega \lambda \cos 1.5\omega T_s + \sin 1.5\omega T_s) \quad (5.5)$$

$F_R(\omega)$ can be defined as [23]

$$F_R(\omega) = \omega \lambda \sin 1.5\omega T_s - \cos 1.5\omega T_s \quad (5.6)$$

To investigate the characteristic of F_R , it is necessary to calculate the values of F_R at special frequency which can be derived as

$$\begin{cases} F_R\left(\frac{\omega_s}{6}\right) = \frac{1}{6} \lambda \omega_s \\ F_R\left(\frac{\omega_s}{3}\right) = 1 \\ F_R\left(\frac{\omega_s}{2}\right) = -\frac{1}{2} \lambda \omega_s \end{cases} \quad (5.7)$$

H is assumed to be positive. According to (5-7), it is can be observed that $F_R(\omega_s/3)$ is positive and $F_R(\omega_s/2)$ is negative, which means there is a certain frequency $\omega_c \in (\omega_s/3, \omega_s/2)$ and $F_R(\omega_c)=0$. Therefore, the region of positive virtual resistance can be extended to ω_c .

Based on the required ω_c and $F_R(\omega_c)=0$, the expression of λ can be calculated as

$$\lambda = \frac{1}{\sqrt{1/LC} \tan 1.5\sqrt{1/LCT_s}} \quad (5.8)$$

Figure 5.7 shows the characteristic of R_{eq2} and X_{eq2} with $\omega_c = 5\omega_s/12$ and $\lambda = 7.643 \times 10^{-5}$.

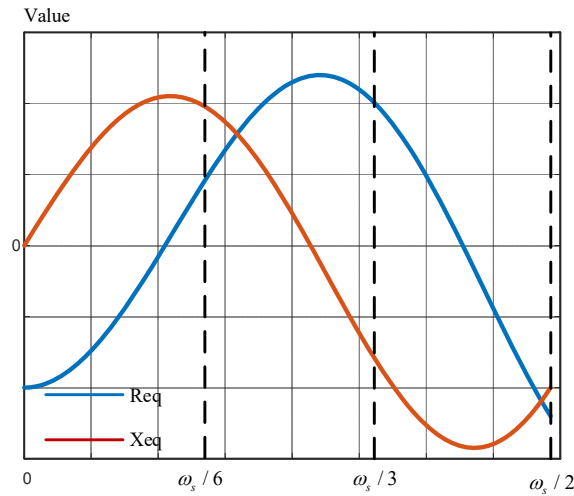


Figure 5.7 Characteristic of R_{eq2} and X_{eq2} with $\lambda = 7.643 \times 10^{-5}$

5.4 Stability analysis

The Backward Euler method is implemented to discrete the negative first-order low-pass filter, which can be attained as[23]

$$GF(z) = GF(s) \Big|_{s=\frac{1-z^{-1}}{T_s}} = -\frac{T_s z}{(\lambda + T_s)z - \lambda} \quad (5.9)$$

The transfer function of open loop transfer function can be calculated as

$$T_{oz}(z) = G_{PR}(z) \cdot \frac{K_{PWM} [(\lambda + T_s)z^2 + T_s z - \lambda] (1 - \cos \omega_r T_s)}{z(z^2 - 2z \cos(\omega_r T_s) + 1)[(\lambda + T_s)z - \lambda] - K_{PWM} \frac{HT_s \sin(\omega_r T_s)}{\omega_r L} (z^2 - z)} \quad (5.10)$$

5.4.1 The effect of H on poles

The denominator of $T_{oz}(z)$ can be extracted from (5.10) as

$$Den(z) = z(z^2 - 2z \cos(\omega_r T_s) + 1)[(\lambda + T_s)z - \lambda] - K_{PWM} \frac{H \sin(\omega_r T_s)}{\omega_r L} (z^2 - z) \quad (5.11)$$

Figure 5.8 shows the Pole map of $Den(z)$ with $\lambda = 7.643 \times 10^{-5}$ when H varies from 0 to 9. According to the results, when $0 < H < 8$, unstable poles do not exist, when $H > 8$, unstable poles exist. Accordingly, we assume $H \in (0, 8)$.

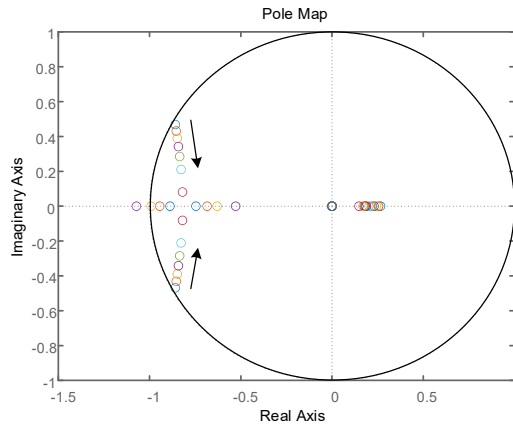


Figure 5.8 Pole map of $Den(z)$ with $\lambda = 7.643 \times 10^{-5}$ when H is changed (Changing from 0 to 9)

5.4.2 -180° crossing

According to the analysis discussed in 5.4.1, there is no unstable poles when $H \in (0, 8)$, which means $P = 0$. Therefore, the system can be stable when

$N^+ - N^- = 0$. **Figure 5.9** shows the bode diagram of $T_{oz}(z)$ with $\lambda = 7.643 \times 10^{-5}$ and $H = 1.2$. As it can be seen, there is no positive crossing and one negative crossing, which means $N^+ = 0$ and $N^- = 1$. Accordingly, if the negative crossing can be invalidated, the system can be stabilized.

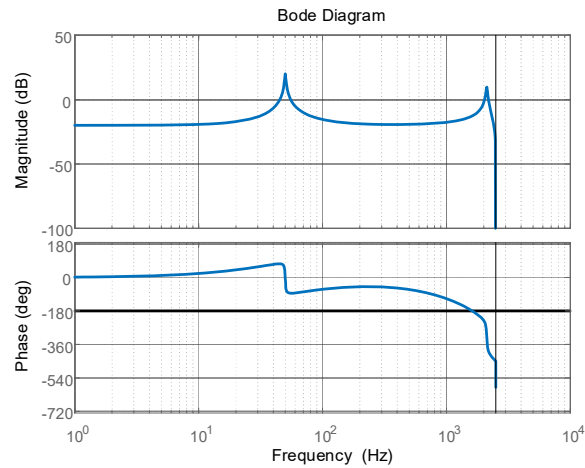


Figure 5.9 The bode diagram of $T_{oz}(z)$ with $\lambda = 7.643 \times 10^{-5}$ and $H = 1.2$

5.5 Parameters design

The easiest way to void the negative crossing is $|T_{oz}(e^{j\omega_r T_s})| < 1$, which can be realized by k_p . To have a stable margin, k_p equals 0.015. **Figure 5.9** shows the corresponding bode diagram.

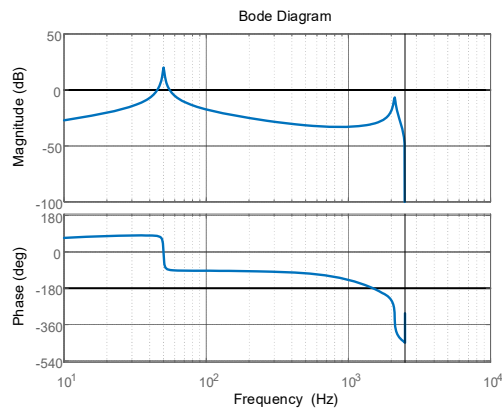


Figure 5.10 the bode diagram of $T_{oz}(z)$ with $\lambda=7.643 \times 10^{-5}$, $H=1.2$ and $k_p=0.015$

Figure 5.10 shows the pole map and the bode diagram when f_r varies from $f_s/6$ to $5f_s/12$. With the same parameters designed at frequency $5f_s/12$, the system still can be stable when resonance frequency varies over a wide range, which is a huge bonus of this proposed method.

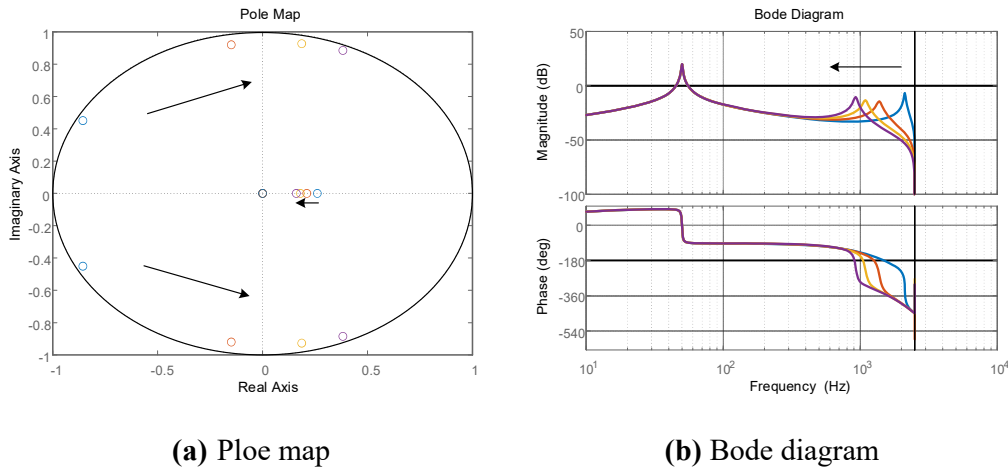


Figure 5.11 The pole map and the bode diagram when f_r changes from $f_s/6$ to $5f_s/12$

5.6 Simulation

To verify the correctness of previous analysis and effectiveness of the proposed parameter design method, the simulation model of the LC-type single-phase off-grid inverter is carried out on PSIM. The experimental parameters are shown in **Table 5-1**.

Table 5-1 Parameters of the off-grid inverter and control parameters

Parameter	Case1	Case 2	Case 3	Case 4	Case 5
Inductor L	1.3 mH				
Capacitor C	5.54 μ F	4.5 μ F	3.71 μ F	12.46 μ F	28 μ F
Resonance frequency f_r	1875Hz	2081	2292Hz	1250Hz	834Hz
DC-side voltage U_{dc}	80 V				
Output voltage U_o	50 V				
The gain K_{PWM}	1				
Sampling frequency f_s	5kHz				
Voltage regular proportional gain kp	0.015				
Voltage regular resonance gain kr	20				
Damping coefficient H	1.2				
λ	7.643×10^{-5}				

Figure 5.12 and **Figure 5.13** show the output waveforms of the inverter and the voltage spectrum when resonance frequency equals $0.9 \times 5f_s / 12$. As it can be seen, the system can be stabilized with negative first-order low-pass filter and the total harmonic distortion is 2.125%.

Figure 5.14 and **Figure 5.15** show the output waveforms of the inverter and the voltage spectrum when resonance frequency equals $5f_s / 12$. The result shows that the system can be stabilized with negative first-order low-pass filter and the total harmonic distortion is 2.65%.

Figure 5.16 and **Figure 5.17** show the output waveforms of the inverter and the voltage spectrum when resonance frequency equals $1.1 \times 5f_s / 12$. As it can be seen, the system can be stabilized with negative first-order low-pass filter and the total harmonic distortion is 3.26%.

Figure 5.18 and **Figure 5.19** show the output waveforms of the inverter and the

voltage spectrum when resonance frequency equals $f_s/4$. The result shows that the system can be stabilized with negative first-order low-pass filter and the total harmonic distortion is 0.91%.

Figure 5.20 and **Figure 5.21** show the output waveforms of the inverter and the voltage spectrum when resonance frequency equals $f_s/6$. The result shows that the system can be stabilized with negative first-order low-pass filter and the total harmonic distortion is 0.4%.

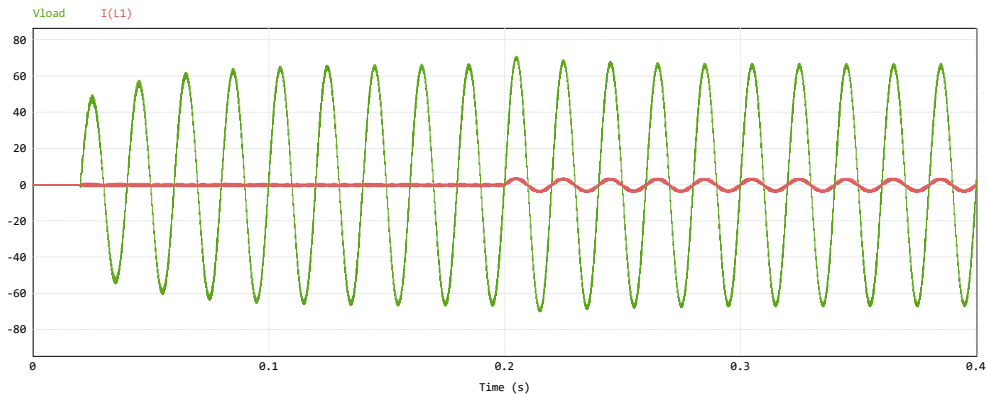


Figure 5.12 Output voltage and load current waveforms of Case 1

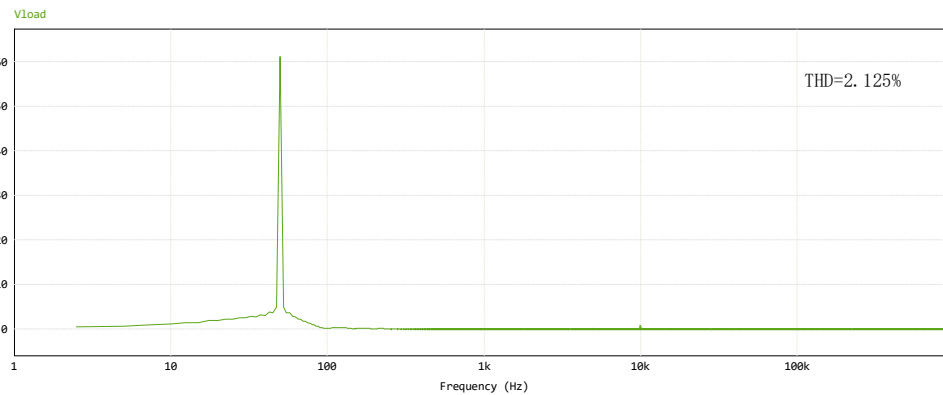


Figure 5.13 Output voltage spectrum of Case 1

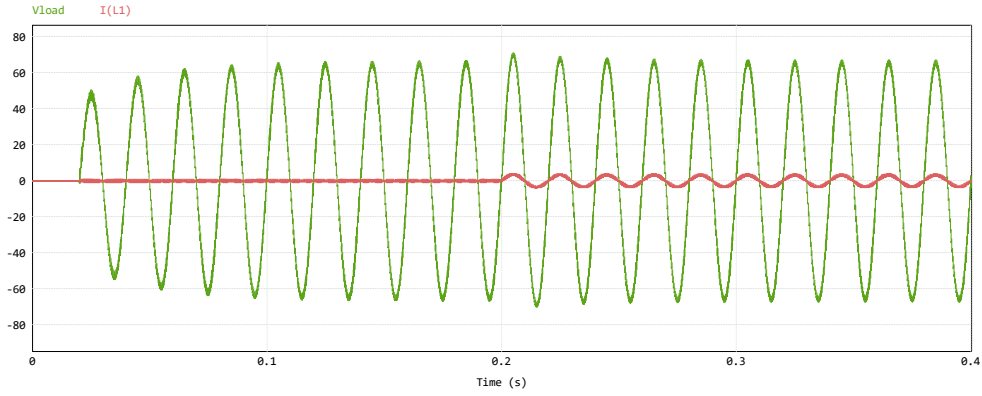


Figure 5.14 Output voltage and load current waveforms of Case 2

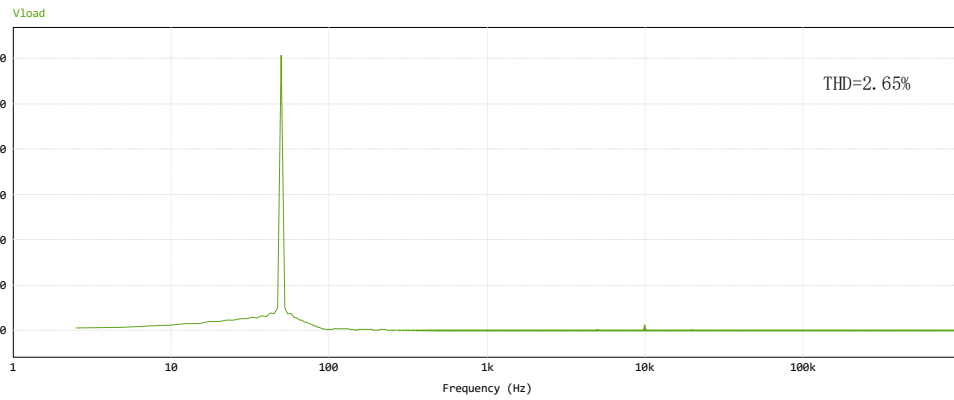


Figure 5.15 Output voltage spectrum of Case 2

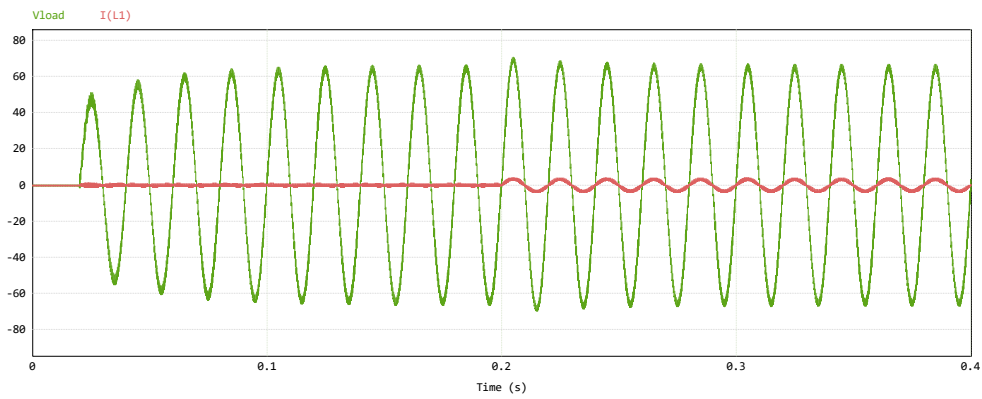


Figure 5.16 Output voltage and load current waveforms of Case 3

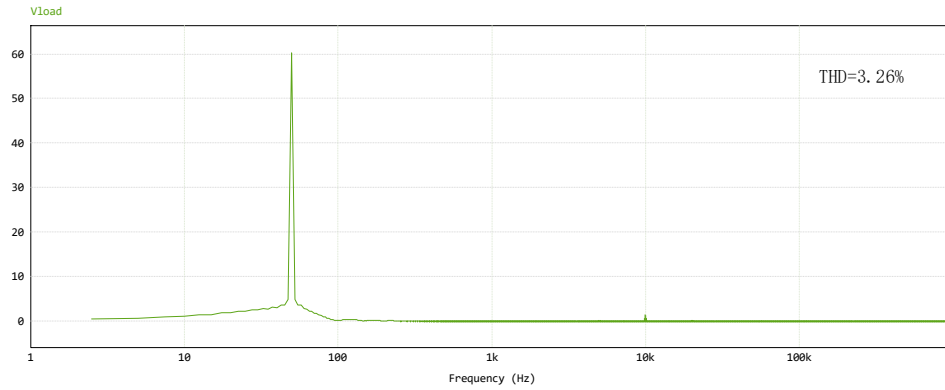


Figure 5.17 Output voltage spectrum of Case 3

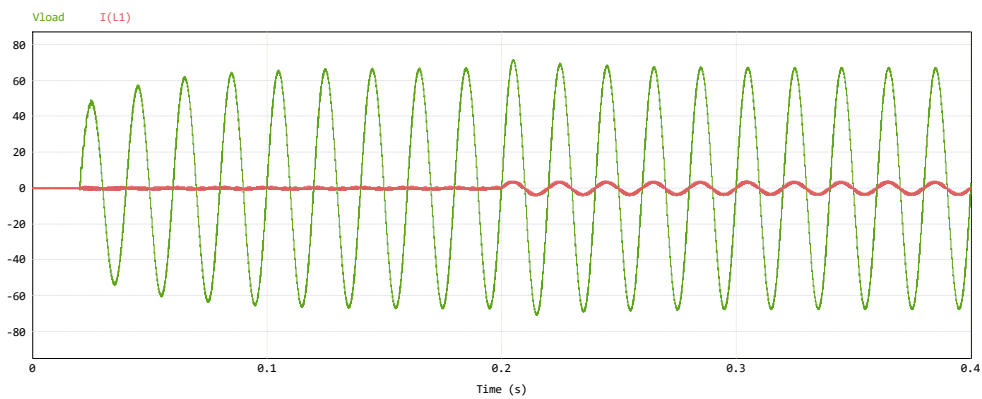


Figure 5.18 output voltage and load current waveforms of Case 4

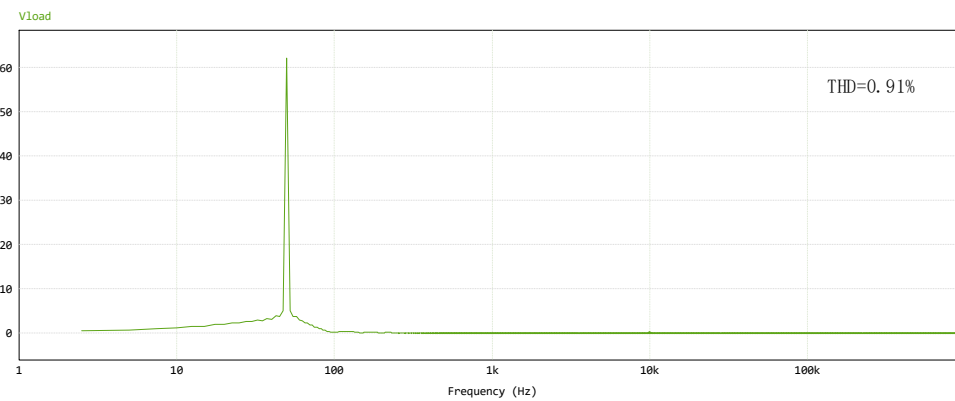


Figure 5.19 Output voltage spectrum of Case 4

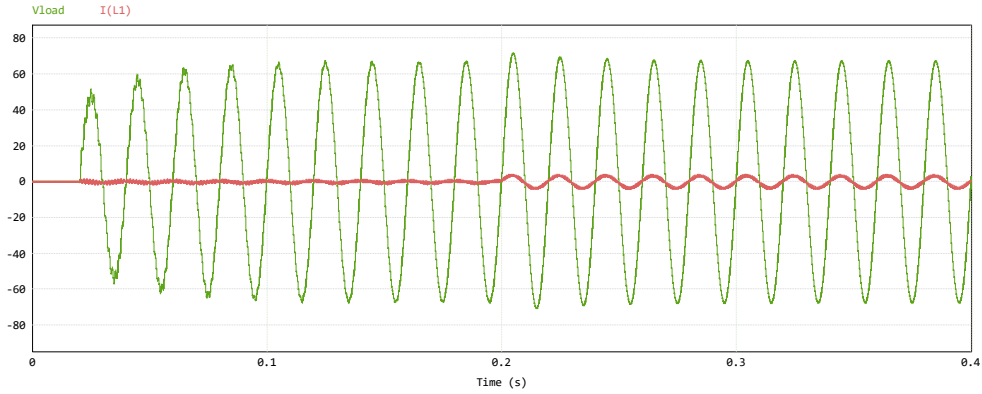


Figure 5.20 Output voltage and load current waveforms of Case 5

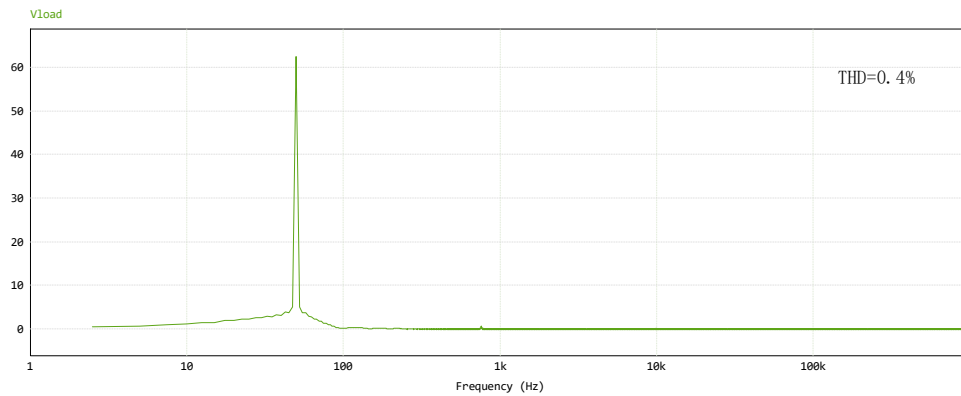


Figure 5.21 Output voltage spectrum of Case 5

5.7 Conclusion

In this chapter, by introducing the Negative First-Order Low-Pass Filter into the capacitor-current feedback branch, the effective damping region can be extended to f_c , where $f_c \in (f_s/3, f_s/2)$. With the same parameters designed at frequency f_c , the system still can be stable when resonance frequency varies over a wide range. Finally, the simulation results verify the effectiveness of this method.

Chapter 6 Thesis conclusion

This thesis primarily discusses the control strategy for LC-type single phase off-grid inverter to extend its effective damping region.

We discuss the power circuit and single control loop of LC-type Off-Grid inverter. The expression of open loop transfer function is obtained through the derivation of each link. According to stability analysis, the system with $kp < |1 - LC(2\pi f_s / 3)^2| / K_{PWM}$ can be stable, when $f_r > f_s / 3$; and the system cannot be stable even with small kp , when $f_r < f_s / 3$, due to the resonance peak. In case $f_r > f_s / 3$, although the system with appropriate control parameters can be stable, the THD cannot satisfy the requirement. If $f_r < f_s / 3$, the system can be stable and at the same time THD can satisfy the requirement through the proposed passive damping approaches in chapter 2. However, considering the energy consumption, passive damping methods is seldom used in high voltage applications.

In contrast with passive damping approaches, active damping methods do not introduce power loss. Thereafter, we investigated, in chapter 3, the stability of the LC-type off-grid inverters with inductor-current feedback active damping when $f_r < f_s / 3$. In the light of stability analysis, three condition combinations are practical to stabilize the system: one precondition (i.e., resonance frequency) and two determined stable conditions. The first combination is frequently chosen so that requirements of THD are satisfied. Notwithstanding, f_r is likely be equal to or greater than $f_s / 6$ in practical applications. When that is true and the two determined stable conditions are untouched, the system will loss stability. Therefore, it is necessary to keep the system stable when

f_r is close to $f_s/6$.

To solve this problem, a Lag compensation method based on all-pass filter is proposed in chapter 4. Although this method can stabilize the system when f_r is close to $f_s/6$, the effective damping region is still narrow.

To sum up, traditional inductor-current feedback active damping can keep system stable when $0 < f_r < f_s/6$ and all-pass filter can stabilize the system when f_r is close to $f_s/6$. In fact, filter parameters sometimes have $\pm 30\%$ error, because of the production process, temperature, component aging, core saturation and other factors. The parameter drift of L and C may cause the resonant frequency to exceed the effective damping region, which will provoke oscillation or even instability. It is proposed an improved inductor-current feedback active damping based on Negative First-Order Low-Pass Filter. By this means, the effective damping region can be extended to f_c , where $f_c \in (f_s/3, f_s/2)$. The system keeps stable when resonance frequency varies over a wide range, with the identical parameters designed at frequency f_c .

References

- [1] Bose B K. Global warming: Energy, environmental pollution, and the impact of power electronics[J]. IEEE Industrial Electronics Magazine, 2010, 4(1): 6-17.
- [2] Sangwongwanich A, Abdelhakim A, Yang Y, et al. Control of single-phase and three-phase DC/AC converters[M]//Control of Power Electronic Converters and Systems. Academic Press, 2018: 153-173.
- [3] Dewan S B, Ziogas P D. Optimum filter design for a single-phase solid-state UPS system[J]. IEEE Transactions on Industry Applications, 1979 (6): 664-669.
- [4] Dahono P A. A control method to damp oscillation in the input LC filter[C]//2002 IEEE 33rd Annual IEEE Power Electronics Specialists Conference. Proceedings (Cat. No. 02CH37289). IEEE, 2002, 4: 1630-1635.
- [5] He J, Li Y W. Generalized closed-loop control schemes with embedded virtual impedances for voltage source converters with LC or LCL filters[J]. IEEE Transactions on Power Electronics, 2011, 27(4): 1850-1861.
- [6] Li Y W. Control and resonance damping of voltage-source and current-source converters with LC filters[J]. IEEE Transactions on Industrial Electronics, 2008, 56(5): 1511-1521.
- [7] Blasko V, Kaura V. A novel control to actively damp resonance in input LC filter of a three-phase voltage source converter[J]. IEEE Transactions on Industry Applications, 1997, 33(2): 542-550.
- [8] Dahono P A, Bahar Y R, Sato Y, et al. Damping of transient oscillations on the output LC filter of PWM inverters by using a virtual resistor[C]//4th IEEE

- International Conference on Power Electronics and Drive Systems. IEEE PEDS 2001-Indonesia. Proceedings (Cat. No. 01TH8594). IEEE, 2001, 1: 403-407.
- [9] Cardenas V M. Digital control in power electronics[C]//2006 IEEE International Power Electronics Congress. IEEE, 2006: xii-xii.
- [10] Geng Y, Yun Y, Chen R, et al. Parameters design and optimization for LC-type off-grid inverters with inductor-current feedback active damping[J]. IEEE Transactions on Power Electronics, 2017, 33(1): 703-715.
- [11] Cha H, Vu T K, Kim J E. Design and control of Proportional-Resonant controller based Photovoltaic power conditioning system[C]//2009 IEEE Energy Conversion Congress and Exposition. IEEE, 2009: 2198-2205.
- [12] Yepes A G, Freijedo F D, Doval-Gandoy J, et al. Effects of discretization methods on the performance of resonant controllers[J]. IEEE transactions on power electronics, 2010, 25(7): 1692-1712.
- [13] Agorreta J L, Borrega M, López J, et al. Modeling and control of N -paralleled grid-connected inverters with LCL filter coupled due to grid impedance in PV plants[J]. IEEE transactions on power electronics, 2010, 26(3): 770-785.
- [14] Lei B, Xiao G C, Wu X L. Comparison of performance between bipolar and unipolar double-frequency sinusoidal pulse width modulation in a digitally controlled H-bridge inverter system[J]. Chinese physics B, 2013, 22(6): 060509.
- [15] Bao C, Ruan X, Wang X, et al. Step-by-step controller design for LCL-type grid-connected inverter with capacitor-current-feedback active-damping[J]. IEEE Transactions on Power Electronics, 2013, 29(3): 1239-1253.

- [16]Li X, Lin P, Tang Y, et al. Stability design of single-loop voltage control with enhanced dynamic for voltage-source converters with a low LC-resonant-frequency[J]. IEEE Transactions on Power Electronics, 2018, 33(11): 9937-9951.
- [17]Dannehl J, Liserre M, Fuchs F W. Filter-based active damping of voltage source converters with LCL filter[J]. IEEE Transactions on Industrial Electronics, 2010, 58(8): 3623-3633.
- [18]Wang X, Lin H, Feng B, et al. Damping of input LC filter resonance based on virtual resistor for matrix converter[C]//2012 IEEE Energy Conversion Congress and Exposition (ECCE). IEEE, 2012: 3910-3916.
- [19]Kim H S, Jung H S, Sul S K. Discrete-time voltage controller for voltage source converters with LC filter based on state-space models[J]. IEEE Transactions on Industry Applications, 2018, 55(1): 529-540.
- [20]Miao Degen. Stability Analysis and Output Voltage Quality Improvement for VSIs with LC Filters[D]. Chongqing: Chongqing University, 2019(in Chinese).
- [21]Zheng K, Zhou L, Long G, et al. A Lag Compensation Method Based on Notch Filter for PV Grid-connected Inverter Under Digital Control[J]. Proceedings of the CSEE, 2019, 39(06):1749-1757+1871(in Chinese).
- [22]Yao W, Yang Y, Xu Y, et al. Phase reshaping via all-pass filters for robust LCL-filter active damping[J]. IEEE Transactions on Power Electronics, 2019, 35(3): 3114-3126.
- [23]Liu H, Bian X, Zhang W, et al. Novel capacitor current feedback active damping strategy for extending the range of equivalent virtual damping [J]. High Voltage

Engineering, 2022,48(01):114-124 (in Chinese).